

Modeling Asymmetric Blade Damage in Quadrotors Through System Identification **Techniques**

Saify, B.; de Visser, C.C.

DOI

10.2514/6.2025-0008

Publication date

Document Version

Final published version

Published in

Proceedings of the AIAA SCITECH 2025 Forum

Citation (APA)

Saify, B., & de Visser, C. C. (2025). Modeling Asymmetric Blade Damage in Quadrotors Through System Identification Techniques. In *Proceedings of the AIAA SCITECH 2025 Forum* Article AIAA 2025-0008 (AIAA Science and Technology Forum and Exposition, AIAA SciTech Forum 2025). American Institute of Aeronautics and Astronautics Inc. (AIAA). https://doi.org/10.2514/6.2025-0008

To cite this publication, please use the final published version (if applicable). Please check the document version above.

Copyright

Other than for strictly personal use, it is not permitted to download, forward or distribute the text or part of it, without the consent of the author(s) and/or copyright holder(s), unless the work is under an open content license such as Creative Commons.

Please contact us and provide details if you believe this document breaches copyrights.

We will remove access to the work immediately and investigate your claim.



Modeling Asymmetric Blade Damage in Quadrotors through System Identification Techniques

B. Saify* and Dr.ir. C.C. de Visser † TU Delft Faculty of Aerospace Engineering Kluyverweg 1, Delft, South Holland, 2629HS

As quadrotors continue to become more popular for personal and commercial use, improving their safety is essential, especially in impaired operating states. With (asymmetric) blade damage (ABD) being a potentially dangerous type of impairment, it is beneficial to understand how it affects the dynamic behavior of a quadrotor. This research examines the effects of blade damage on the dynamic model of a quadrotor through system identification techniques. Time scale separation is used to split the low-frequency aerodynamic behavior and high-frequency (HF) dynamics. Aerodynamic models are identified using stepwise regression, and a novel approach for modeling HF dynamics –relying purely on onboard sensors– using spectral analysis and simplex B-splines has been developed. A majority of the aerodynamic models surpass R^2 values of 0.95, and the HF models exceed R^2 values of 0.90. The findings provide new insights and implications for diagnosing ABD in quadrotors.

I. Nomenclature

 \mathcal{F}_I = inertial frame \mathcal{F}_B = body frame

 p_I = quadrotor inertial position vector v_B = quadrotor body frame velocity vector

q = quadrotor attitude vector

 ω_b = quadrotor angular velocity vector in the body frame

u, v, w = forward, lateral, and vertical velocity components in the body frame respectively

 ϕ, θ, ψ = roll, pitch, and yaw angles respectively p, q, r = roll, pitch, and yaw rates respectively F_B = external force vector in the body frame M_B = external moment vector in the body frame

 R_{IB} = transformation matrix from body to inertial frame

 K_{IB} = matrix which maps body frame angular rates ω_b to inertial attitude rates \dot{q}

 Ω_i = rotational speed of rotor *i*

T = thrust

 v_i = induced velocity y = observation vector θ = parameter vector A = regressor matrix

 $F_{x,y,z}$ = aerodynamic force components in the body frame $M_{x,y,z}$ = aerodynamic moment components in the body frame

 $\mu_{x,y,z}$ = advance ratios

II. Introduction

QUADROTORS are one of the most popular unmanned aerial vehicle (UAV) configurations in use, owing to their simplicity and versatility [1]. With these systems starting to gain traction in the commercial sector, safe operability has come under scrutiny. This is corroborated by the vast amount of research focused on improving the safety and

^{*}PhD Candidate, Faculty of Aerospace Engineering, Aerospace Structures and Materials, TU Delft, b.saify@tudelft.nl

[†]Associate Professor, Faculty of Aerospace Engineering Control&Simulation, TU Delft

reliability of these systems. Key areas of research include safe control algorithms in the event of system impairments [2–4], diagnosis of faults [5, 6], aerodynamic modeling [7–9] and safe flight envelope prediction [10].

Several fault scenarios can inflict quadrotors, with actuator faults being one of the most commonly researched due to the high impact of such faults on controllability. Actuator faults in quadrotors are split into two sub-categories; motor failures, and physical damage to the propeller blades. Control of quadrotors subject to complete motor failures has been treated thoroughly [2–4]. The diagnosis of partial losses in rotor effectiveness has also been researched [5, 11, 12]. The latter fault condition is characterized by physical damage to the propeller blades while the motor driving the damaged propeller remains in good health. Physical blade damage has also received considerable attention in the literature both in terms of robust control [13–15], as well as fault diagnosis [16–18].

Physical propeller damage is one of the important modes of structural failure which can adversely affect a quadrotor and is the focus of this paper. Physical damage on a single propeller is divided into two categories; symmetrical and asymmetrical. The former is characterized by equal extent and type of damage to each propeller blade. Naturally, asymmetric damage is characterized by different levels of damage to each propeller blade. It can be argued that asymmetric damage is worth investigating more than symmetric damage purely from the point of view that such a fault condition is more likely to occur, which is also confirmed to some qualitative extent through the experiments of Brown et al. [19].

Several approaches to the diagnosis of (a)symmetric blade damage have been proposed in literature [17, 18, 20–22]. Most approaches for diagnosing blade damage rely on data gathered using an Inertial Measurement Unit (IMU), a ubiquitous sensor found on quadrotors because it is essential for state estimation and control. The most common approaches to ABD diagnosis involve transforming the time-series IMU data to the frequency domain. This of course makes intuitive sense because the circular –and therefore periodic– motion of the propeller blades results in salient features in the frequency domain. Many methods use features extracted directly from the time domain [18] or frequency domain [17, 23] to train neural-network-based classifiers. Notably, Brown et al. [19] thoroughly examine a slew of potential sensors for blade damage diagnosis such as thermal measurements of the electronic speed controllers (ESC), accelerometer measurements, current sensors, and battery voltage to name a few. However, they determined that the accelerometer is one of the best options for ABD diagnosis.

While several works focus on the diagnosis of ABD, no example was found where the effects of blade damage are modeled through system identification techniques. Neither the effects on the aerodynamics nor the high-frequency effects of ABD on quadrotors are thoroughly studied through data-driven analysis. This paper aims to bridge this gap in knowledge. This is achieved by performing experiments with quadrotor platforms subject to ABD at varying levels. Data gathered from these experiments is used to build aerodynamic models and hybrid mass-aerodynamic high-frequency models to capture the effects of ABD. The aim of these models is twofold; for one they allow for accurate simulations and therefore model-based prediction of safe flight envelopes of quadrotors afflicted with blade damage, and to examine the effects of varying locations and levels of blade damage on aerodynamic model parameters as well as the parameters of the models of the high-frequency phenomenon caused by mass and aerodynamic imbalances.

The paper outline is as follows. Fundamentals of the quadrotor platform are introduced in Sec. III, the methodology for experimentation, and modeling are outlined in Sec. IV and the results are presented in Sec. V. Section VI provides a discussion of the findings, limitations, and potential of the methodology, followed by a conclusion in Sec. VII.

III. Quadrotor Fundamentals

A. First Principles Model

The kinematics and simplified dynamics of a quadrotor are introduced based on first principles and simple relations for propulsive force and moments. A quadrotor is 6 degree-of-freedom (DOF) system, in that it can control its position and attitude in 3D space. Two reference frames are used when defining the equations of motion of a quadrotor; the inertial frame and the body-fixed reference frame. The inertial frame \mathcal{F}_I is aligned with respect to the Earth such that the xy plane is parallel to the ground, and the xz plane contains the Earth's axis of rotation. The Earth is assumed locally flat and non-rotating (which is quite common for quadrotor analysis) resulting in the inertial frame being chosen arbitrarily as long as the z-axis is perpendicular to, and points into, the ground. The body frame \mathcal{F}_B is defined as depicted in Fig. 1 and is centered at the center of gravity of the quadrotor.

Let $p_I = [x \ y \ z]^T$ and $v_B = [u \ v \ w]^T$ represent the inertial position and body frame velocities of a quadrotor respectively. Similarly, let $q = [\phi \ \theta \ \psi]^T$ and $\omega_B = [p \ q \ r]^T$ represent the attitude of the quadrotor and angular rates in the body frame respectively. Note that the attitude vector q essentially describes the orientation of \mathcal{F}_B with

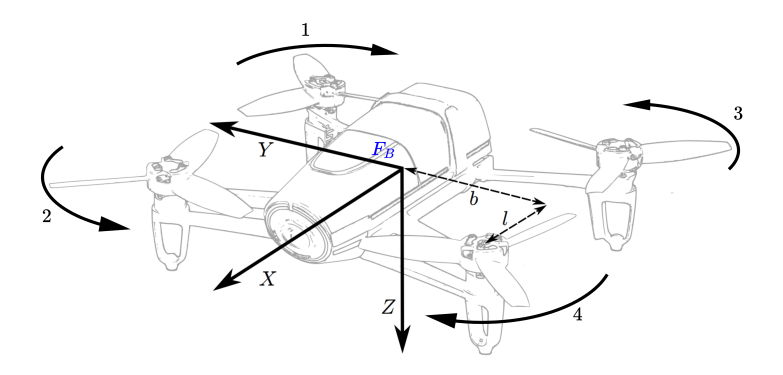


Fig. 1 Representation of a quadrotor body frame and rotation directions of rotors [24]

respect to \mathcal{F}_I using Euler angles ϕ , θ , and ψ to represent roll, pitch, and yaw respectively. The matrix R_{IB} describes the transformation from the body frame velocities to the inertial velocities using the Euler angles. Similarly, K_{IB} kinematically relates body angular rates to inertial attitude rates. Constructions for these matrices can be found in [25].

With the aforementioned quantities defined, the equations of motion (EOM) of the quadrotor –split into the linear and rotational EOM– can be formally introduced. Linear motion is described by Eq. (1) and Eq. (2) while rotational motion is described by Eq. (3) and Eq. (4). The terms F_B and M_B represent the external forces and moments acting on the quadrotor in \mathcal{F}_B respectively which are influenced by the effects of gravity, propulsion, and aerodynamics. This simple model excludes the gyroscopic effects of the spinning rotors, and these effects are not included for the remainder of the paper because their contribution was found to be negligible compared to the aerodynamic moments.

$$\dot{\boldsymbol{p}}_{I} = \boldsymbol{R}_{IB} \boldsymbol{v}_{B} \tag{1}$$

$$\dot{\mathbf{v}}_B = \frac{1}{m} \mathbf{F}_B + \omega_B \times \mathbf{v}_B \tag{2}$$

$$\dot{q} = K_{IB}\omega_B \tag{3}$$

$$\dot{\boldsymbol{\omega}}_{B} = \boldsymbol{I}^{-1} \left(\boldsymbol{M}_{B} - \boldsymbol{\omega}_{B} \times \boldsymbol{I} \boldsymbol{\omega}_{B} \right) \tag{4}$$

A simple model is added to the first principles model to account for the thrust force and propulsive control moments created by the 4 rotors. Equation (5) describes the propulsive thrust generated as a result of the rotational speed Ω_i of each rotor, and Eq. (6) describes the propulsive moments on each axis in \mathcal{F}_B as a function of rotor speeds and the geometry of the quadrotor (see Fig. 1 for rotor numbering, rotation direction, and geometrical definitions of parameters l and l0). The parameters l0 are the thrust and torque constants of the propeller respectively.

$$\boldsymbol{F}_{B,p} = \begin{bmatrix} 0 \\ 0 \\ -\kappa_0 \sum \Omega_i^2 \end{bmatrix} \tag{5}$$

$$\mathbf{M}_{B,p} = \begin{bmatrix} b\kappa_0((\Omega_1^2 + \Omega_2^2) - (\Omega_3^2 + \Omega_4^2)) \\ l\kappa_0((\Omega_2^2 + \Omega_4^2) - (\Omega_1^2 + \Omega_3^2)) \\ -\tau_0 \sum \Omega_i^2 \mathrm{sign}(\Omega_i) \end{bmatrix}$$
(6)

B. Extensions to the Quadrotor Model

The simple quadrotor model is only applicable around the hovering flight condition and fails to capture quadrotor behavior in high-speed flight. Therefore, it has been extended in the literature by borrowing from helicopter theory [9, 26]. These extensions describe the aerodynamic forces and moments generated by a quadrotor in moderate to

high-speed flight. The most important effects are identified to be thrust variance, blade flapping, and induced drag [9, 25–28].

Thrust variance describes the dependence of thrust (of a single rotor) on the incoming flow velocity V and angle of attack α of the rotor plane with respect to the incoming flow. The thrust equation can be derived from both momentum theory and blade element theory to yield Eq. 7 and Eq. 8 respectively where A is rotor disk area, a the blade airfoil lift-slope, b the number of blades, c the chord, R the rotor radius, ω the propeller rotational speed, and θ the blade pitch angle. These relations were used by Sun et al. [7, 29] to inform candidate model regressor choices for quadrotor model identification.

$$T = 2\rho A v_i \sqrt{V^2 + 2V v_i \sin \alpha + v_i^2} \tag{7}$$

$$T = \frac{\rho a b c \omega^2 R^3}{2} \left(\frac{\theta}{3} + \frac{V^2 \cos^2 \alpha \theta}{2\omega^2 R^2} + \frac{V \sin \alpha + v}{2\omega R} \right)$$
 (8)

Blade flapping is another important phenomenon that affects quadrotors in translational flight and is not accounted for by the first principles model. Blade flapping occurs when the velocity field at a blade changes as a function of the azimuth angle of the blade, for example in forward flight where the advancing blade experiences a higher velocity than the retreating blade. The imbalance in the velocity field induces forces that cause the rotor plane, and thus the thrust vector, to tilt such that it is no longer perpendicular to the actuator (motor) axis. This effect has been analyzed thoroughly in helicopter literature [30] and has been adopted to explain quadrotor body forces that occur in the *xy* plane. The tilting of the thrust vector also induces aerodynamic pitching moments depending on how far the c.g. of the quadrotor is from the plane containing the 4 rotors.

The flap angle β of a blade is defined as a function of the azimuth Ψ using Eq. 9 where a_0 is the coning angle a_{1s} and b_{1s} are the tilt angles of the rotor plane orthogonal to, and along the in-plane velocity vector of the rotor. These angles can be calculated using Eq. 10 and Eq. 11 [27]. The values of parameters A and B are determined by the physical characteristics of the propeller. With the known thrust and tilt of the rotor plane due to flapping, the thrust vector can be projected into the xy body plane of the quadrotor to predict drag forces and resultant moments. In addition to moments caused by in-plane drag-like forces at the rotor, the stiffness of the rotor blades also induces moments directly at the rotor axis. This moment is computed using Eq. 12 [27].

$$\beta = a_0 - a_{1s}\cos\Psi + b_{1s}\sin\Psi \tag{9}$$

$$a_{1s} = \frac{|V_p|}{\Omega R} A_{1c} + \frac{1}{\Omega} B_2 p - \frac{1}{\Omega} B_1 q \tag{10}$$

$$b_{1s} = -\frac{|V_p|}{\Omega R} A_{1s} + \frac{1}{\Omega} B_1 p - \frac{1}{\Omega} B_2 q \tag{11}$$

$$M_{bs} = k_{\beta} a_{1s} \tag{12}$$

IV. Modeling Methodology

The presence of ABD is assumed to show effects in two separable frequency regions; the low-frequency region, and the high-frequency region. Damaged propellers experience a loss in thrust capability due to a decrease in blade surface area, which subsequently impacts the dynamic ability of the quadrotor. This loss of thrust affects the low frequency (<60 Hz) dynamic behavior of the quadrotor such as the ability to produce control moments, and accelerations in the z body axis.

The high-frequency effects of asymmetric damage are caused by imbalances in the mass, and aerodynamic forces acting on the damaged propeller. These effects are dominant in the frequency range of the motor rotational speed, which is roughly an order of magnitude higher than the dynamics of the quadrotor as a whole. For example, the hover frequencies of the propellers on the chosen experimental platforms are in the range of 280 Hz to 350 Hz and can go up to 550 Hz at the maximum throttle setting, which is much higher than the cut-off frequency of the slow-speed quadrotor dynamics when no blade damage is present. This assumption is further solidified by Sun et al. [31] who use a cut-off frequency of only 20 Hz for identifying aerodynamic models for a quadrotor comparable in size and

Table 1 Damage location abbreviations

Damage location	Front	Back	Right	Left
Abbrevitaion	F	В	R	L

mass to the experimental quadrotor platforms used in this research. Using the assumption of time-scale separation, the low-frequency aerodynamic effects, and high-frequency mass-aerodynamic imbalance effects occurring due to ABD are modeled separately.

This section outlines the techniques used to model the aerodynamic models, and high-frequency dynamics models for quadrotors with ABD. The damage cases tested in this research are defined in Sec. IV.A. The experimental platforms used for the research are presented, and practical considerations are discussed in Sec. IV.B. The methodology utilized to construct the low-frequency aerodynamic models and high-frequency models is explained in Sec. IV.C and IV.D respectively.

A. Damage Scenarios

1. Damage Case Definitions

Figure 2 shows propellers artificially inflicted with asymmetric damage. The damage is introduced as a straight cut along the blade chord (at each radial location). The damage level is defined as *the missing blade span as a percentage of propeller radius*. Only damage to a single blade was tested. Additionally, both the Beetle and Geyser use the same type of propeller.



Fig. 2 Damage cases tested (left to right): Healthy - 10% - 15% - 20% - 25% - 30% - 40%

Damage scenarios are described with respect to the damage level, and which propeller on the quadrotor is inflicted. The nomenclature 'level' location' is used to describe these damage scenarios. The location is a composition of abbreviations listed in Table 1 while level is the extent of the damage.

The *location* for a damage scenario where a single propeller is damaged is defined by combining the longitudinal location followed by the lateral location. For example, damage to the front-right propeller is defined by location identifier 'FR'. If there are two propellers damaged on the same side, then the location identifier is simply the abbreviation of that side. For example, 'F' would be the identifier for both front propellers being simultaneously damaged.

The *level* is simply the percentage damage of the propeller(s). For example, 30% damage to the front-right propeller is represented as 30FR, while 30% damage to both front propellers is represented by 30F. It must be noted here that the nomenclature scheme defined here does not account for simultaneous damage to more than two propellers, damage to non-adjacent propeller pairs, or damage scenarios where adjacent propellers have different *levels* of damage. While these damage scenarios are possible, they are qualitatively assumed less likely, especially ones where diagonally opposite propellers are damaged. In addition to reducing the experimental costs, the aforementioned reasons are cited for the choice of tested damage scenarios.

2. Damage Cases Tested

The damage cases covered by the aerodynamic models and HF models of the Beetle quadrotor are listed in Table 2 and 3 respectively. Damage cases with simultaneous damage to two propellers are not covered by the HF models of the Beetle, while they are included in the aerodynamic models. The reason for this is further elaborated on in Sec. VI. The aerodynamic models for the various damage cases are constructed both for hovering flights, as well as flights with a

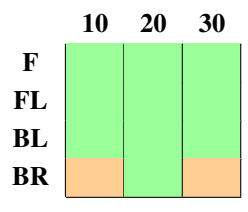
mean airspeed of 8 m/s to capture high-speed effects.

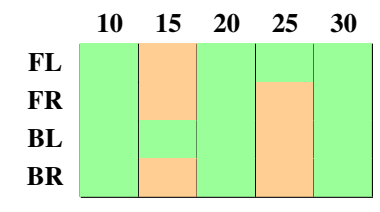
Table 4 shows the cases covered by the HF models of the Geyser drone. These cases are much more sparsely covered when compared to the HF models of the Beetle. The reason for this is that the Geyser drone was treated as a secondary platform to apply the HF modeling methodology which gave very good results on the Beetle. The aerodynamic models of the Geyser were not identified because it was only used to test the HF modeling approach and how it generalizes to different quadrotors.

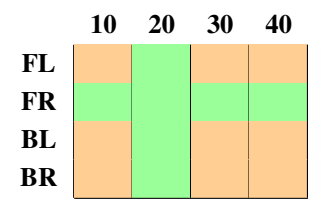
Table 2 Damage scenarios tested for Beetle aerodynamic modeling

for Beetle HF modeling

Table 3 Damage scenarios tested Table 4 Damage scenarios tested for Geyser HF modeling







B. Experimental Platform and Practical Considerations

1. Platform and Facilities

Two quadrotors were used for experimentation shown in Fig. 3a and 3b with their respective code names. These quadrotors are built using off-the-shelf hobby (kits and parts) and use open source flight control software Betaflight * The inertia properties of the Beetle quadrotor are presented in Table 5. The inertia properties of the Geyser are not presented because these were not required for HF model identification however they are in the same order of magnitude as the Beetle.

The experimental flights were conducted in the Open Jet Facility[†] and the CyberZoo[‡]. The former is a large low-speed wind tunnel that can produce steady wind at up to 35 [m/s] and features a nozzle with dimensions 2.85 x 2.85 m. The latter is a large caged arena used for testing robotic systems. These facilities are found at the Aerospace Engineering Faculty of the TU Delft. Both facilities feature an optical motion capture (mo-cap) system 'Optitrack' § which was used as an external data source to provide accurate measurements of the pose of the quadrotors. Looking at Fig. 3a, the special reflective tape used by the Optitrack system to track the quadrotor can be seen pasted at various locations around the frame.

2. Practical Limitations

One of the key practical limitations was the difficulty in gathering the required sensor data. Construction of the aerodynamic models requires high-frequency sampling of the rotational speeds of each of the motors while modeling the high-frequency effects requires high-rate raw (unfiltered) data from the IMU. Betaflight is capable of logging high-rate motor speed data, raw accelerometer data, or raw gyroscope data simultaneously because of the inherent limitations of the firmware. However, concurrent logging of all three of these sources of data is required to simultaneously gather data for low-frequency and high-frequency modeling.

Table 5 Inertia properties of the Beetle (including battery)

Mass [kg]	Mome	nt of Inertia [kg m ²]
	I_{xx}	I_{yy}	I_{zz}
3.770E-01	8.998E-04	9.158E-04	1.467E-03

^{*}https://github.com/betaflight/betaflight

https://www.tudelft.nl/lr/organisatie/afdelingen/flow-physics-and-technology/facilities/low-speed-windtunnels/open-jet-facility

[†]https://tudelftroboticsinstitute.nl/labs/cyber-zoo

^{\$}https://optitrack.com/

Alternatively to Betaflight, $PX4^{\P}$ was compatible with the flight controllers used in both experimental quadrotors and provided the capability to log all required on-board data simultaneously. However, the motor speeds are measured in PX4 via the telemetry line connecting the ESC to the flight control board unlike Betaflight which uses the more advanced "bidirectional DShot". Therefore, the logging rate of motor speeds in PX4 is limited to 32 Hz while Betaflight can log motor speeds at up to 2 kHz.

Due to the unique data collection limitations of each of the flight firmware, a compromise was made. Data for low-frequency aerodynamic modeling was gathered using Betaflight, while that for high-frequency modeling was gathered using PX4. This is possible because these models are assumed, and observed to be, separable in the frequency domain as was explained earlier. One disadvantage to this approach is of course that double the flights have to be performed, however, this was a manageable limitation.

Another practical limitation comes from the fact that flying with ABD causes severe vibrations which tend to saturate the IMU, and also can cause the motors to fail over time. It was found that blade damage at or above 40% causes enough clipping in the accelerometer, that the attitude estimate gets biased over time, making the quadrotor very difficult to fly in angle mode. Motor failures were also observed to be more frequent at higher than 30% damage for the Beetle quadrotor. For these reasons, the highest used in the experimental flights was 30% for the Beetle, while the Geyser—having a higher mass, and better motors—could be reliably flown at 40% damage.

The clipping in the IMU also means that accelerations of the quadrotor caused by low-frequency aerodynamic forces —which we are trying to model— can not be measured accurately. Even at lower damage levels, where clipping is not present, the filtering of accelerometer data performed by Betaflight results in erroneous spikes in the accelerometer measurements. To resolve this, the pose measurements obtained from the Optitrack system were used to compute the accelerations in the body frame. Due to the exceptional position accuracy of the Optitrack system (< 1mm) and low measurement noise, double time-differentiation of the position measurements using a 2nd order Savitzky-Golay filter [32] gives accurate acceleration estimates. Surprisingly, the accelerations derived from Optitrack position measurements show similar noise performance as IMU measurements. An advantage of using Optitrack-derived accelerations is that no filtering takes place. We however still cannot rely on these acceleration measurements for high-frequency modeling because the sampling frequency of 120 Hz is not nearly as high as the 8 kHz sampling rate of the IMU, and the oscillations in position and attitude resulting from the high-frequency forces and moments result in pose changes which cannot be detected by Optitrack system. Thus, the Optitrack system is used to measure the accelerations which are then used to build the low-frequency aerodynamic models while IMU-derived accelerations are used for modeling the high-frequency behavior.

Unlike the accelerometer, the gyroscope is much more resilient against the vibrations caused by ABD. The limits of the gyroscopes on both the Beetle and Geyser are 2400 o /s, while the oscillations caused by the worst-case vibrations are not more than around 400 deg/s in magnitude. Therefore, the flight controller, and standard PID-based flight control algorithms of Betaflight and PX4 are able to accurately control the angular rates around all three body axes of the quadrotor. The lack of clipping in the gyroscope also meant that the moments acting on the quadrotor body could be recovered directly unlike the accelerations which were derived from the Optitrack pose measurements. The moments M_B acting on the quadrotor are derived using Eq. 4 where $\dot{\omega}_B$ is computed through numerical differentiation of the measured angular rates using a 2^{nd} order Savitzky-Golay filter.

C. Aerodynamic Model Identification with Stepwise Regression

1. State estimation

In order to build accurate models, the states that are used as dependent variables are estimated. This is done using a Extended Kalman Filter (EKF) [33]. As explained in Sec. IV.B, the accelerations of the quadrotor are measured using the external mo-cap system because of severe vibration-induced clipping of the on-board accelerometers rendering these measurements unusable. Similarly, velocity is also reconstructed from the Optitrack position measurements. This results in all measurements in terms of linear dynamics (Eq 1 and 2) coming from a single source. This essentially means that the measurements must be taken as ground truth, and no state estimation is performed here. This is assumed reasonable because of the exceptional position measurement performance of the Optitrack system.

Unlike linear accelerations and velocities, the angular rates and attitude can both be measured through independent sources of data. The IMU provides angular rate data, while the attitude is measured with the Optitrack system. These

[¶]https://github.com/PX4/PX4-Autopilot





(a) Beetle (b) Geyser

Fig. 3 The quadrotor platforms used for collecting experimental data.

sources of data are fused together using rotational kinematics (Eq. 3). The measurement model for all three attitude angles and angular rates assumes additive white Gaussian noise, the statistics of which were determined through analysis of stationary IMU and Optitrack measurements.

2. Parameter estimation

Aerodynamic models were identified using the stepwise regression (SWR) technique [32] which was earlier used by Sun et al. [29]. A global linear-in-the-parameters polynomial model of the from shown in Eq. 13 is used to model the dependent variable $\mathbf{y} \in \mathbb{R}^n$ as a combinations of regressors $A = \begin{bmatrix} 1 & \boldsymbol{\xi}_1 & \boldsymbol{\xi}_2 & \dots & \boldsymbol{\xi}_p \end{bmatrix} \in \mathbb{R}^{n \times p}$ with model parameters $\boldsymbol{\theta} \in \mathbb{R}^p$ and residuals $\boldsymbol{\epsilon} \in \mathbb{R}^n$. The optimal parameters using an Ordinary Least Squares estimator $\hat{\boldsymbol{\theta}}$ are computed using Eq. 14.

$$y = A\theta + \epsilon \tag{13}$$

$$\hat{\boldsymbol{\theta}} = \left(A^T A \right)^{-1} A^T \mathbf{y} \tag{14}$$

The SWR approach, in addition to determining the optimal model parameters, also determines the set of regressors that best describe the dependent variable. The regressors are added and removed from a pool of regressors in a step-wise manner until a stopping criterion is met. An example of a candidate regressor pool of independent variables x_1 , x_2 , and x_3 to model dependent variable y is shown in Eq. 15 where $P_1^2(x_1, x_3)$ represents all second-order polynomials in x_1 and x_3 and $P_2(x_1, x_2)$ [1 x_3] represent all polynomials in x_1 and x_2 multiplied by 1 or x_3^2

$$y = P_1^2(x_1, x_3) + P_2(x_1, x_2) [1 x_3^2]$$
(15)

The SWR procedure is described next. First, the model is initialized with a bias vector $A = \begin{bmatrix} 1 & 1 & 1 \end{bmatrix}^T$. Then, the following algorithmic loop is entered:

- 1) The optimal OLS parameters are estimated using Eq. 14 and the residuals ϵ for this model are computed.
- 2) Each regressor ξ_i in the remaining pool of regressors is made orthogonal to the current model using Eq. 16.

$$\lambda_{i} = \xi_{i} - A \left(A^{T} A \right)^{-1} A^{T} y \tag{16}$$

- 3) The orthogonalized regressor λ_j with the highest correlation to the model residuals is found, and the corresponding regressor ξ_i is added to the model (A), and removed from the candidate pool.
- 4) The model regressors in A are statistically evaluated through an F test. Given q regressors in the current model, the partial F-ratio for the k_{th} regressor is calculated using Equation 17 where s^2 is the variance of the fit error computed using Equation 18 for N data points.

$$F_0 = \frac{SS_R(\hat{\boldsymbol{\theta}}_q) - SS_R(\hat{\boldsymbol{\theta}}_{q-k})}{s^2}$$
 (17)

$$s^2 = \frac{\epsilon^T \epsilon}{N - q - 1} \tag{18}$$

 $SS_R(\hat{\theta}_q)$ is the regression sum of squares for the current model, and $SS_R(\hat{\theta}_{q-k})$ is the same but with regressor ξ_k removed from the model. The SS_R value is computed using Equation 19 where \bar{y} is the mean of the observation vector.

$$SS_R = \hat{\boldsymbol{\theta}}^T A^T \mathbf{y} - N \bar{\mathbf{y}} \tag{19}$$

If the regressor with the smallest F_0 value has an F score below a constant threshold F_{out} , then that regressor is removed. The algorithm stops if the regressor removed is the same as the one added in that loop. We use an F_{out} threshold of 4 as was done by Sun et al. [7]

5) A stopping criteria based on the Predict Square Error (PSE) (Eq. 20) is used to terminate the algorithm. The first term in this equation is the model residual mean squared error, and the second term penalizes model redundancy where q is the number of regressors in the current model. Over-fitting leads to an increase in the PSE at which point the SWR algorithm is terminated.

$$PSE = \frac{1}{N} \epsilon^T \epsilon + \sigma_{max}^2 \frac{q}{N} \tag{20}$$

3. Flight Test Maneuvers

The system-identification test flights were flown manually. However, to ensure that the data gathered for all damage cases are similar, a set of identical pre-planned maneuvers was flown for each damage case. While the exact flight path followed during each maneuver cannot be kept consistent through this approach, the excitation of all forces and moments can be generated to cover similar envelopes.

The longitudinal flight and lateral flight maneuvers were kept largely separated by design, which means that forces and moments in the x and y body axes were seldom excited simultaneously. This was mainly because of difficulties in flying such maneuvers manually. This results in the '+' shape of the plot showing the kernel density estimates of the distribution of (F_x, F_y) and (M_x, M_y) in Fig. 4 and Fig. 5 respectively.

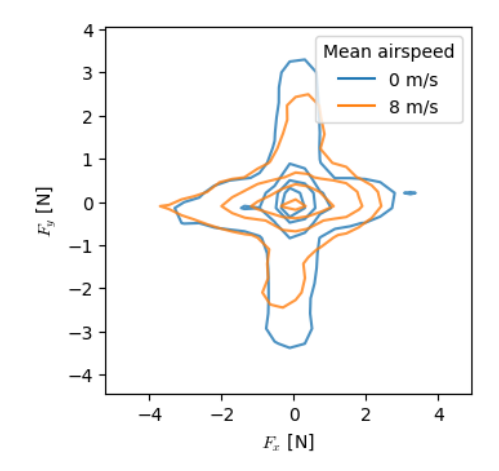


Fig. 4 Kernel density estimates of the force distributions in the xy body plane

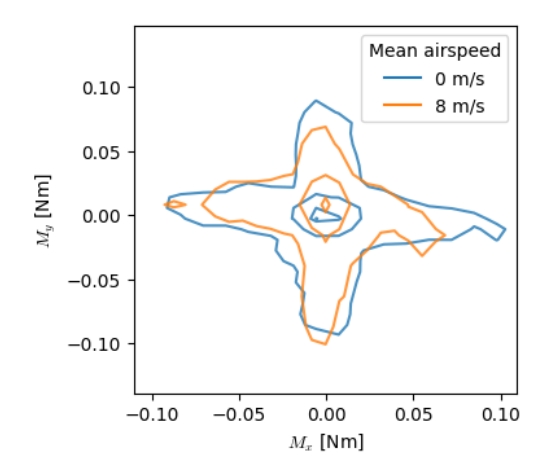


Fig. 5 Kernel density estimates of the moment distributions in the xy body plane

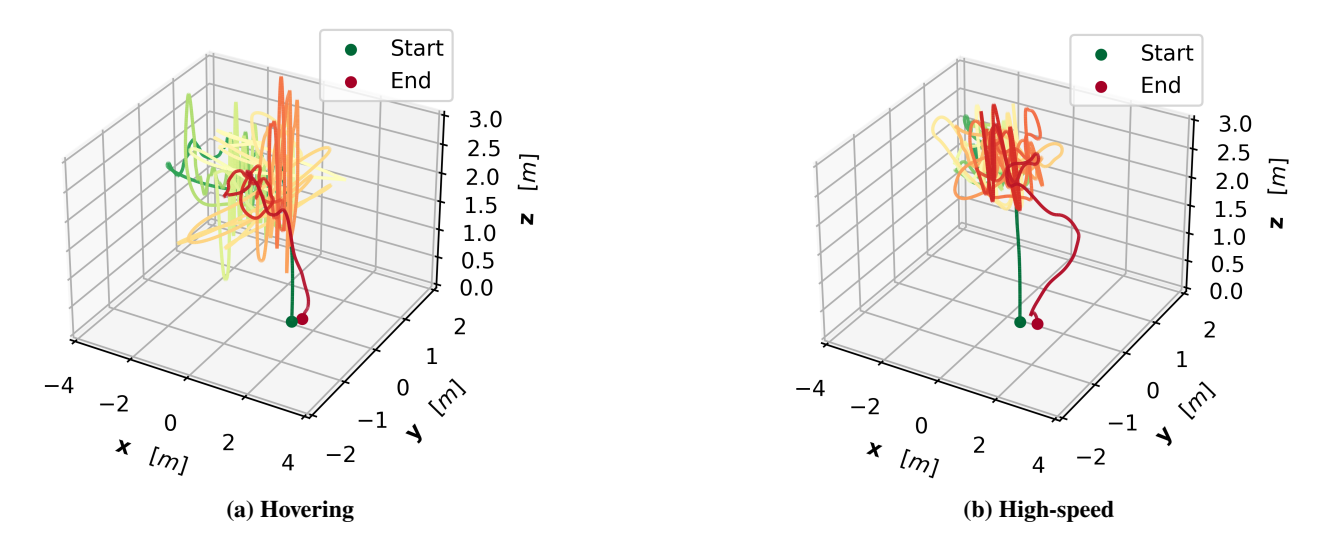


Fig. 6 Example trajectories of system identification test flights for hovering (left) and high-speed flight (right)

Figure 6a and Fig. 6b show examples of the spatial trajectories followed for a flight without wind, and at a wind speed of 8 m/s respectively. The system identification flight maneuvers, consisting of fast pitch, roll, and throttle inputs, as well as slow (sustained) pitch, roll, and throttle inputs, are visible in the figures. While yaw maneuvers were tried for hovering flights, it was difficult to manually excite the yawing moments, which also led to poor yawing moment models. In high-speed flight, only fast roll maneuvers were possible to execute while staying within the wind stream, and yawing maneuvers were not performed.

4. Model Candidates

With the goal of creating models for all three body forces, and all three body moments using SWR, first a set of candidate regressors is chosen. These sets include various measured states, such as body velocities, angular rates, attitude, as well as control inputs which are derived from measured motor speeds. The choice of candidate regressors is also influenced by the theoretical equations for thrust, and additional effects explained in Sec. III.B. A limit of 3 added regressors was imposed for all models because it was found that after this point, regressors become increasingly complex while offering insignificant improvements to model performance.

 $F_x = X_0 + X_1 u$

$$+ P^{3}(u, w) \left[1, \omega_{tot}, q, u_{q}, \sin(\theta), \cos(\theta) \right]$$

$$+ P^{2}(\mu_{x}, \mu_{z}) \left[1, \omega_{tot}, q, u_{q}, \sin(\theta), \cos(\theta) \right]$$

$$+ P^{2}(q) \left[1, \omega_{tot} \right]$$

$$+ P^{2}(u_{q}) \left[1, \sin(\theta), \cos(\theta), \omega_{tot} \right]$$

$$+ P^{2}(\omega_{tot}) \left[\sin(\theta) \right]$$

$$F_{y} = Y_{0} + Y_{1}v$$

$$+ P^{3}(v, w) \left[1, \omega_{tot}, p, u_{p}, \sin(\phi), \cos(\phi) \right]$$

$$+ P^{2}(\mu_{y}, \mu_{z}) \left[1, \omega_{tot}, p, u_{p}, \sin(\phi), \cos(\phi) \right]$$

$$+ P^{2}(p) \left[1, \omega_{tot} \right]$$

$$+ P^{2}(u_{p}) \left[1, \sin(\phi), \cos(\phi), \omega_{tot} \right]$$

$$+ P^{2}(\omega_{tot}) \left[\sin(\phi) \right]$$

$$(22)$$

$$F_{z} = Z_{0} + Z_{1}w$$

$$+ P^{3}(|u|, |v|, w) [1, \omega_{tot}, |p|, |q|, |u_{p}|, |u_{q}|]$$

$$+ P^{2}(|\mu_{x}|, |\mu_{y}|, \mu_{z}) [1, \omega_{tot}, |p|, |q|, |u_{p}|, |u_{q}|]$$

$$+ P^{2}(\omega_{tot}) [1]$$

$$+ P^{2}(|p|, |q|, |r|) [1, \omega_{tot}]$$
(23)

Equations 21, 22, and 23 show the model candidate structures for the x, y, and z body axis forces respectively. Equations 24, 25, and 26 show the model candidates for the x, y, and z body moments respectively. Note that coupling between F_x and F_y was largely eliminated while choosing these regressor sets because the flight test maneuvers were largely uncoupled in the longitudinal and lateral directions. The regressor ω_t ot is defined as the sum of the rotor speeds, and the input roll, pitch, and yaw control moments $-u_p$, u_q and u_r are defined according to the respective axis-specific rotor speed combinations defined in 6. The advance ratios, $\mu_{x,y,z}$, are added to capture the effects of thrust variance as well as blade flapping.

While the attitude angles are not necessarily a good regressor choice from a physical sense, they are found to improve model performance significantly, likely because these angles encode information about relative flow angles with respect to the rotors of the quadrotor. It is important to point out here that while the chosen model candidates are influenced by analytical models of the underlying physical phenomena, they do not necessarily capture cause-effect relationships, but rather also model correlations that describe reality from a phenomenological perspective. Nevertheless, when applied to quadrotors (and other aerospace systems), these models can still offer a reliable means to make predictions, even if the underlying physics is not exactly captured.

$$M_{x} = L_{0} + L_{1}p + L_{2}u_{p}$$

$$+ P^{3} (|u|, v, w) \left[1, \omega_{tot}, p, |r|, u_{p}, |u_{r}|, \sin(\phi), \cos(\phi) \right]$$

$$+ P^{2} (|\mu_{x}|, \mu_{y}, \mu_{z}) \left[1, \omega_{tot}, p, |r|, u_{p}, |u_{r}|, \sin(\phi), \cos(\phi) \right]$$

$$+ P^{2} (p, |q|, |r|) \left[1, \omega_{tot}, \sin(\phi), \cos(\phi) \right]$$

$$+ P^{2} (u_{p}, |u_{q}|, |u_{r}|) \left[1, \sin(\phi), \cos(\phi), \omega_{tot} \right]$$

$$+ P^{2} (\omega_{tot}) \left[\sin(\phi), \cos(\phi) \right]$$
(24)

$$M_{y} = M_{0} + M_{1}q + M_{2}u_{q}$$

$$+ P^{3}(u, |v|, w) \left[1, \omega_{tot}, q, |r|, u_{q}, |u_{r}|, \sin(\theta), \cos(\theta) \right]$$

$$+ P^{2}(\mu_{x}, |\mu_{y}|, \mu_{z}) \left[1, \omega_{tot}, q, |r|, u_{q}, |u_{r}|, \sin(\theta), \cos(\theta) \right]$$

$$+ P^{2}(|p|, q, |r|) \left[1, \omega_{tot}, \sin(\theta), \cos(\theta) \right]$$

$$+ P^{2}(u_{q}, |u_{p}|, |u_{r}|) \left[1, \sin(\theta), \cos(\theta), \omega_{tot} \right]$$

$$+ P^{2}(\omega_{tot}) \left[\sin(\theta), \cos(\theta) \right]$$
(25)

$$M_{z} = N_{0} + N_{1}r + N_{2}u_{r}$$

$$+ P^{3} (|u|, |v|, w) \left[1, \omega_{tot}, |p|, |q|, |r|, u_{p}, |u_{q}|, |u_{r}|, \sin(\theta), \cos(\theta), \sin(\phi), \cos(\phi) \right]$$

$$+ P^{2} (|\mu_{x}|, |\mu_{y}|, \mu_{z}) \left[1, \omega_{tot}, |p|, |q|, |r|, u_{p}, |u_{q}|, |u_{r}|, \sin(\theta), \cos(\theta), \sin(\phi), \cos(\phi) \right]$$

$$+ P^{2} (|p|, |q|, r) \left[1, \omega_{tot} \right]$$

$$+ P^{2} (|u_{q}|, |u_{p}|, u_{r}) \left[1, \omega_{tot} \right]$$

$$+ P^{2} (\omega_{tot}) \left[\sin(\theta), \cos(\theta), \sin(\phi), \cos(\phi) \right]$$

$$(26)$$

5. Model Simplification

Rather unsurprisingly, SWR often finds a different set of regressors (for each force and moment model) for different damage cases. However, these regressors tend to often be spurious and offer almost insignificant model improvement. Additionally, two regressors that are highly correlated may be picked somewhat randomly from one damage case to another.

To gain a better understanding of the variation of model parameters with the extent of blade damage, simplifications were made to the models found through SWR. In this way, the polynomial models for all damage cases have the same set of regressors, and only the parameter values for these regressors change for different damage cases.

The exact procedure for picking the fixed regressors was largely heuristic. The general rules-of-thumb are; to keep the regressors that appear most commonly for all damage scenarios, offer the most significant model improvements, and are not highly correlated with other regressors. Following these procedures, the models could be simplified without losing too much performance, but allow for better physical insights into how the impact of a given regressor changes with blade damage, and if any clear patterns can be found.

D. High-Frequency Model Identification

1. General Approach

The goal of the High-frequency models is to be able to reproduce the IMU signals which are measured by a quadrotor inflicted with ABD. The base assumption used for constructing the high-frequency models is that the time series of each IMU measurement can be modeled as a sum of a few sinusoids. This assumption is physically motivated by the fact that force and moment imbalances created by an asymmetrically damaged propeller will be cyclic in nature, and visual examination of the measured IMU signals also shows that this is the case (see Fig. 21). Therefore, the model structure shown in Eq. 27 was chosen, where k is the number of harmonics of the frequency f, and d_l is the damage level of the propeller. To parameterize this model, the amplitude surface A_n of the n^{lh} harmonic is constructed as a function of f and d_l .

$$y(t) = \sum_{n=1}^{k} A_n(f, d_l) \sin(2\pi n f t)$$
 (27)

The amplitude models were built assuming dependence only on the frequency and level of damage. Here, frequency refers to the rotational speed of the damaged propeller in Hz, and corresponding harmonics. This choice of dependent variables is again due to physical reasoning. For one, higher levels of damage result in larger mass imbalances as well as larger asymmetries in the aerodynamic forces and torques generated by the damaged propeller. It is straightforward to see that the mass imbalance of a damaged propeller induces a net centripetal force vector which oscillates in direction at the rotational frequency of the rotor. These forces can be quite high even with small mass imbalances because the propellers of the quadrotor spin at very fast speeds. A first principles approach would be to model the centripetal forces as scaling with the square of the rotational speed of the propeller, but this ignores various physical interactions that can be captured through data-driven analysis.

A less obvious high-frequency effect comes from the aerodynamic imbalances of the damaged rotor. For example, in the presence of ABD, the thrust force is no longer aligned with the rotational axis of the propeller but is offset from this axis and also rotates around it in sync with the propeller. Due to its movement with respect to the center of gravity of the quadrotor, the thrust imbalance induces oscillatory pitching and rolling moments around the quadrotor c.g. Similar to the imbalance in thrust, there is also an in-plane drag force generated perpendicular to the rotation axis with some offset. The moment arm of this imbalanced drag force also oscillates sinusoidally with respect to the c.g., resulting in oscillatory yawing moments created around the quadrotor c.g. The spinning drag force vector, similar to the centripetal forces due to the mass imbalance, also causes oscillatory forces in the *x* and *y* body axes of the quadrotor.

The forces and moments described earlier do not consider the structural frame of the quadrotor, and how this frame affects the measurements taken at the IMU. The frames of both the Beetle and Geyser quadrotors are largely made of carbon composites, meaning they are quite stiff. However, no structure is infinitely stiff, and therefore as the oscillatory forces and torques of the damaged rotor are transmitted through the frame, they get altered due to structural resonance in the frame. Even the stand-offs that are used to mount the flight controller to the frame of the quadrotor affect the forces before they are measured by the IMU which is soldered on the flight control board. Clearly, there are complex interactions with the structural frame of the quadrotor which are very difficult to model from first principles. However, using a data-driven method, the effects of frame resonance get lumped along with all the other physical interactions that take place in the presence of ABD.

Finally, another kinematic consideration to keep in mind is that the IMU does not lie exactly at the c.g. of the quadrotor. This offset means that the IMU does not measure the accelerations of the c.g. of the drone, but rather the accelerations which are also corrupted by rotational rates and rotational accelerations about the c.g. While this effect can be analytically corrected, there is no good reason to do so. It is again re-emphasized that the goal of the

high-frequency models is to accurately inject the lumped effects of oscillatory forces and torques arising due to ABD on the measurements made by the IMU, not to accurately model the forces and torques themselves. These models can then facilitate the accurate reproduction of high-frequency effects in simulations of quadrotors with damaged propellers.

The flight maneuvers flown to sufficiently excite the high-frequency phenomenon described above were chosen with the simple requirement of making sure the damaged propeller goes through a large part of the rotational speed range of the motor. This essentially means that the maneuvers should be flown such that the full throttle range is covered. This proved challenging in an indoor environment because of the restricted space for mobility. This problem was overcome by performing short, yet aggressive successive throttle punches, as well as longer duration throttle pulses with lower maximum throttle input. In addition to the above, aggressive rolling and pitching maneuvers were also performed to again ensure that the damaged propeller covers a large part of the rotational speed range of the motor within a single flight. The cumulative distribution of motor frequencies over all the test flights of the Beetle is shown in Fig. 36.

2. Spectral Analysis

Before identifying a model to predict the amplitudes of sinusoidal oscillations measured by the IMU, the amplitudes and corresponding frequencies must be estimated from the time-series data of each IMU axis. This can also be interpreted as the 'state estimation' step of identifying the high-frequency models.

There are a handful of techniques that can be used to transform signals from the time domain to the frequency domain. However, for this application, some important constraints must be considered while choosing a method. For one, the IMU time series signal generated during a flight will be non-stationary, therefore an evolutionary spectrum must be computed. Another practical constraint is that the sampling times of the IMU are not perfectly constant, which may pose additional challenges. With these constraints, a spectrogram constructed using the short-time Fourier transform (STFT) was used. The SciPy implementation of the STFT was used for the analysis presented in this paper [34]. Even though this technique assumes evenly sampled data, the amount of sampling jitter observed in the experimental data was not severe enough to significantly impact the results. This was also numerically verified by computing STFTs of artificially generated sinusoidal signals with greater amounts of jitter than what was observed in the experimental data. A detailed analysis of the noise and jitter properties of IMU measurements is presented in Appendix A.

Two important parameters of the spectrogram are the window length (n_s), and the number of samples ($n_{\rm fft}$) used to compute the STFT at each time slice. The window length, in combination with the sampling frequency f_s , sets the frequency resolution (f_r) of the spectrogram, while ($n_{\rm fft}$) essentially sets the amount of zero-padding applied to each time slice of the signal being analyzed. While zero-padding does not surpass the frequency resolution limit, it does generate more frequency bins in the STFT. The resulting frequencies are no longer orthogonal to each other, however, which means that two sinusoids with frequency separation within the frequency resolution of the STFT cannot be resolved perfectly. The IMU signals are comprised mainly of a few dominant sinusoids which are separated by several multiples of the frequency resolution. Thus, zero-padding allows for better recovery of the properties of the sinusoids comprising the signal compared to the no-zero-padding case.

To visualize the effect of zero padding, a numerical example is shown in Fig. 7. Here, a 0.02 s long signal ($f_r = 50 \text{ Hz}$) with a sampling frequency of 4 kHz (N = 80) and comprising of three pure sinusoids was generated. By zero-padding the signal with $n_{\text{fft}} = 2000$, an effective frequency resolution of 2 Hz is achieved. It is clear from Fig. 7 that applying zero-padding facilitates interpolation between the frequencies corresponding to the true frequency resolution. However, this comes at the cost of spurious peaks caused by the fact that the sin functions at the zero-padded frequencies do not form an orthogonal set. Using a Hann window solves this problem at the expense of broadening the peaks. Fortunately, this is not a problem for the spectral analysis of IMU signals because these are dominated by a base sinusoid with a minimum frequency generally above 100 Hz, and its harmonics have frequency separations greater than or equal to this value.

The values of the parameters n_s and $n_{\rm fit}$ are linked to parameters f_r , f_{r_e} and the sampling frequency f_s through Eq. 28 and 29 respectively. The choice of f_r and f_{r_e} plays a critical role in determining the quality of the STFT. If the f_r is chosen to be small, equating to large time windows, the signal may go through a large change in frequency within the time window resulting in the frequency content being smeared across multiple frequencies. Therefore, the true frequency-amplitude relationship cannot be recovered. Alternatively, a large value for f_r , equating to very short time windows may again be detrimental as there is little information in each window. Since the main factor influencing the choice of these parameters is how fast the dominant frequencies of the signal change with time, a numerical study was conducted (described in detail in Appendix B) which resulted in a choice of 60 Hz for f_r and 2 Hz for f_{r_e} .

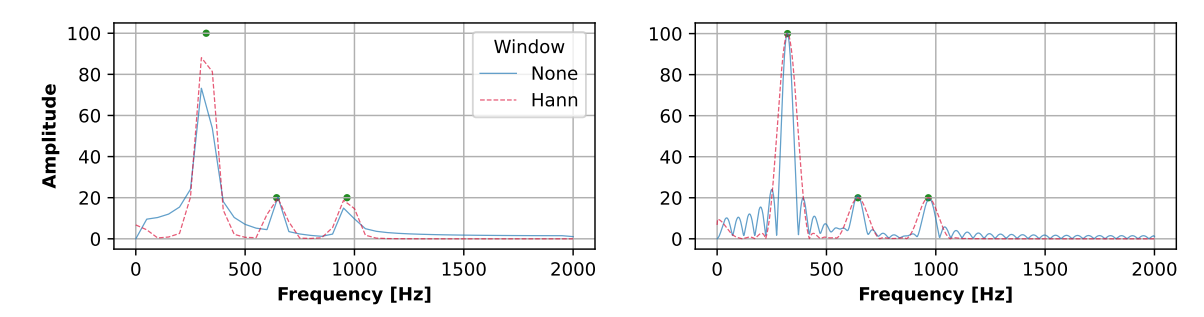


Fig. 7 Comparison of STFT computed without zero padding (left) to that with zero-padding (right) where the circular markers show the true underlying frequencies and associated amplitudes of the time-series signal.

$$n_s = \text{floor}\left(\frac{f_s}{f_r}\right) \tag{28}$$

$$n_{\rm fft} = {\rm floor}\left(\frac{f_s}{f_{r_e}}\right)$$
 (29)

Once the spectrogram of a signal is computed, each slice of the spectrogram is analyzed to find the location of the peak frequency, its harmonics, and the respective amplitudes of these harmonics. This procedure results in a data set of frequency-amplitude pairs for all the dominant harmonics of the time signal. Since the base harmonic is expected to be near the measured motor rotational speed, this frequency is found by locating the highest peak within a certain frequency range f_{range} of the motor frequency. The value of f_{range} is set to 25 Hz, which is heuristically set to ensure that a large range of frequency around the motor frequency is checked for peaks. With the frequency of the base harmonic known, the same procedure is repeated for the higher harmonics. Figure 8 shows an example of the spectral analysis described above applied to the raw roll rate measurements obtained from the Geyser drone. Here the motor frequency went from around 160 Hz to above 350 Hz in this span of 0.15 seconds, which is visible in the spectrogram. The detected amplitudes of the base harmonic are shown along with the addition of the amplitudes of the 2^{nd} and 3^{rd} harmonics, which collectively bound the signal fairly accurately. The significance of the 2^{nd} harmonic is also evident in this particular set of frequencies. It is important to note here that the harmonics above the first are only computed for base harmonic frequencies which ensure a frequency separation of at least $3f_r$ (180 Hz) because smearing in the peaks of the STFT results in inaccurate estimates of amplitudes with low separation between sinusoids. Because the harmonics do not have significant contributions below (roughly) 250 Hz, this is not a major limitation.

3. Simplex B-splines

The final step of the system identification of the HF models is to fit a surface to each of the amplitude-frequency-damage scattered estimates for each harmonic, of each IMU signal, for all damage locations tested to obtain models of the form A_n (f, d). Because of the highly non-linear local features of these surfaces, Simplex B-splines [35, 36] are used as the curve-fitting method of choice. Global polynomial models were also tried but did not give satisfactory results. Here, simplex B-splines are briefly summarised.

Simplex B-splines comprise of basis polynomials, defined locally over simplices t_i belonging to a triangulation \mathcal{T} , which are joined together to satisfy some prescribed continuity condition between polynomials of neighboring simplices. Simplices contain a local coordinate system known as Barycentric coordinates $\boldsymbol{b} = (b_0, ..., n_n) \in \mathbb{R}^{n+1}$ which uniquely map to point in \mathbb{R}^n . Given some point \boldsymbol{x} inside a simplex with vertices $(v_0, ..., v_n)$ where $v_i \in \mathbb{R}^n$, Eq. 30 relates the barycentric coordinates to \boldsymbol{x} . The barycentric coordinates $b_i \geq 0$ if \boldsymbol{x} is inside the simplex.

$$x = \sum_{i=0}^{n} b_i v_i \tag{30}$$

The B-form polynomials are defined in barycentric coordinates on a simplex according to Eq. 31 where c_{κ} are the B-coefficients of the polynomial set indexed with multi-index $\kappa = (\kappa_0, ..., \kappa_n) \in \mathbb{R}^n$ defined such that $|\kappa| = \sum_i \kappa_i$, $\kappa! = \prod_i \kappa_i$, and $\boldsymbol{b}^{\kappa} = \prod_i b_i^{\kappa_i}$ [35]. Each permutation of κ corresponds to a unique B-from polynomial and its

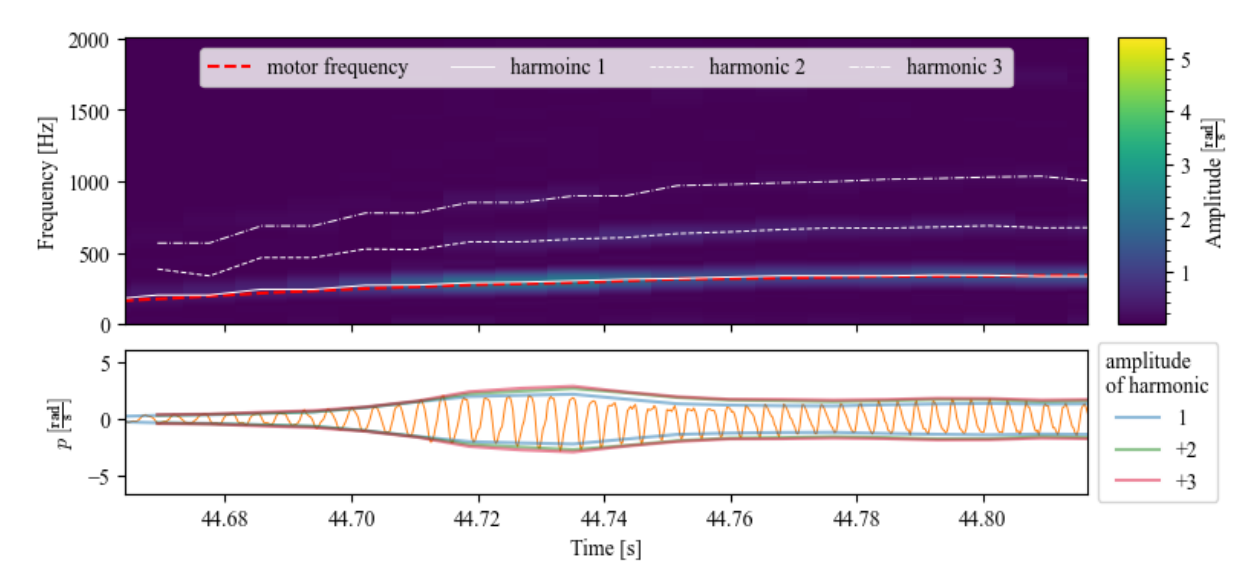


Fig. 8 A time-snippet of the roll rate (bottom) measured by the Geyser quadrotor for damage case 30FR, and the spectrogram of this signal showing peak harmonics related to the motor frequency (top).

B-coefficient, and the collective set forms a basis for the space spanned by all B-form polynomials of degree d in n variables.

$$p(\boldsymbol{b}) = \sum_{|\kappa|} c_{\kappa} \frac{d!}{\kappa!} \kappa \tag{31}$$

A continuity order r between B-form polynomials of neighboring simplices t_i and t_j are enforced through constraints on the respective B-coefficients of the two simplices using Eq. 32 where $\gamma = (\gamma_0, ..., \gamma_n)$ is another multi-index independent of κ , and w is the out-of-edge vertex. The continuity conditions for all simplices in the triangulation can be compiled into matrix form as shown in Eq. 33 where H is known as the 'smoothness matrix' [35].

$$c_{(\kappa_0,\dots,\kappa_{n-1},m)}^{t_i} = \sum_{|\gamma|=m} c_{(\kappa_0,\dots,\kappa_{n-1},0)+\gamma}^{t_j} B_{\gamma}^m(w), \quad 0 \le m \le r$$
(32)

$$Hc = 0 (33)$$

Given a pair of observations (x_i, y_i) related by some function f such that $y_i = f(x_i) + \epsilon_i$ where ϵ_i is a residual term. Then, the regression model for approximating f using a linear combination of B-form polynomials with degree d defined over a triangulation of f simplices is given by Eq. 34 where f are the barycentric coordinates of f with respect to simplex f. This expression can be written in matrix form to include all observations f through a data sifting matrix f which ensures that observations are only active within the simplices that contain them, explained in further detail by de Visser et al. [35]. The final spline-based regression model is then given by Eq. 35 where f is the vector of observations and f and f is the local regression matrix of all observations. Finally, the OLS estimation problem cost function is formulated as shown in Eq. 36. The equality-constrained OLS parameter estimator f using Lagrange multipliers f is then given by Eq. 37.

$$y_{i} = \sum_{j=1}^{J} \sum_{|\kappa|=d} c_{\kappa}^{t_{j}} B_{\kappa}^{d} (b_{i}) + \epsilon_{i}$$
(34)

$$Y = Xc + \epsilon \tag{35}$$

$$J_{OLS}(\mathbf{c}) = \frac{1}{2} (\mathbf{Y} - \mathbf{X}\mathbf{c})^T (\mathbf{Y} - \mathbf{X}\mathbf{c}) \text{ subject to } \mathbf{H}\mathbf{c} = 0$$
 (36)

$$\begin{bmatrix} \hat{\mathbf{c}} \\ \hat{\lambda} \end{bmatrix} = \begin{bmatrix} \mathbf{X}^T \mathbf{X} & \mathbf{H}^T \\ \mathbf{H} & 0 \end{bmatrix}^{+} \cdot \begin{bmatrix} \mathbf{X}^T \mathbf{Y} \\ 0 \end{bmatrix}$$
(37)

Simplex B-splines require the user to define a triangulation, the degree d, and continuity order r. These parameters are set based on the intuitive physical reasoning of the system being modeled, and certain best practices. In general, it is advised to start with a few simplices, low polynomial degree, and continuity order, and increase the complexity henceforth. For the amplitude surfaces presented in this paper, certain important aspects of the data must be considered when choosing a triangulation, degree, and continuity order. For one, the data are concentrated along the direction of frequency, while very sparse in the direction of damage level (see Fig. 27a). Secondly, the data is not uniformly scattered in the $f - d_l$ plane, but rather constrained in linear regions corresponding to each damage level. Because of these properties, a triangulation that is dense in the direction of f but sparse in the direction of f is chosen. An example is shown in Fig. 27a with 20 equally sized triangles. It is clear to see from the models presented in Sec V.B that the local nonlinearities in the observed data are present along f, which is a further reason for more triangles along this direction. B-form polynomials with degree 3 and 1st order continuity were used to construct simple models that still capture the observed nonlinearities in the data.

A point to note is that the high-frequency models include both the blade damage level and frequency as regressors instead of building 1-dimensional spline models at each damage level separately. Surfaces are fit in the $f - d_l$ plane rather than curves for each damage level separately so that the amplitude models can facilitate the prediction of HF behavior at damage levels in between the rows of experimental data. An alternative approach to interpolate between damage levels would be to construct one-dimensional models as a function of frequency at all damage levels. Then, the corresponding B-coefficient parameter values of curves at the different damage levels can be interpolated to create interpolated spline curves. While there is no concrete proof that the applied method is better than this alternative, it does offer a more natural solution to the problem.

V. Results

A. Aerodynamics Models

1. Stepwise regression Models

Tables 6 and 7 respectively present the model performance metrics of the SWR force and moment models constructed for the low-speed flight regime. Tables 8 and 9 respectively present the model performance metrics for the force and moments models identified for the high-speed flight regime. It is evident that all the low-speed force and moment models give very good performance except for the yawing moment model, which was difficult to excite during the system-identification test flights. For high-speed flight, all the models perform worse except for M_x , with F_x and M_y particularly worse than the other models. Overall, however, all the models give decent performance and can be used for simulation purposes. The ratio of training data to test data was 75:25 for all the models. The similarity between the metrics for the test and the complete set shows that the models do not overfit the data.

To examine whether the SWR models actually capture the effects of blade damage, a 'model confusion matrix' was constructed. This matrix is constructed for each force and moment model, for all damage cases. The models for each damage case are applied to the observed data of all damage cases, and the NRMSE is computed for all combinations. Each row of the matrix represents the SWR model of the damage case, while the columns represent the training data for the damage case. With the matrix of NRMSE values computed, the relative NRMSE R_{NRMSE} values of the off-diagonal elements are computed with respect to the corresponding diagonal elements through Eq. 38. Based on this definition, if the off-diagonal elements have values above 1, this means that the model from one damage case fits the data of another damage case better, while values below 1 suggest the opposite.

$$R_{NRMSE_{ij}} = \frac{NRMSE_{ij}}{\min(NRMSE_{ii}, NRMSE_{jj})}$$
(38)

Figures 9 and 10 show the model confusion matrices for the low-speed and high-speed aerodynamic models respectively. These are computed by averaging (element-wise) the confusion matrices of each force and moment model. The results show that models applied to off-diagonal elements can have significantly lower NRMSE values, suggesting that the models for each damage case capture the effects of blade damage on the aerodynamics of the quadrotor. However,

Table 6 Model performance metrics of aerodynamic force models around hover

		F	7 _x			F	, y		F_z				
Case	NRMSE		\mathbb{R}^2		NRI	MSE	R	\mathbb{R}^2	NRI	MSE	R	R ²	
	Full	Test	Full	Test	Full	Test	Full	Test	Full	Test	Full	Test	
Healthy	0.106	0.107	0.989	0.989	0.111	0.109	0.988	0.988	0.081	0.080	0.993	0.994	
10F	0.117	0.118	0.986	0.986	0.090	0.090	0.992	0.992	0.077	0.078	0.994	0.994	
10BL	0.157	0.157	0.975	0.975	0.087	0.086	0.992	0.993	0.080	0.081	0.994	0.993	
10FL	0.113	0.110	0.987	0.988	0.125	0.125	0.984	0.984	0.125	0.125	0.984	0.984	
20F	0.129	0.125	0.983	0.984	0.100	0.102	0.990	0.990	0.062	0.062	0.996	0.996	
20BL	0.125	0.118	0.984	0.986	0.079	0.078	0.994	0.994	0.065	0.065	0.996	0.996	
20BR	0.086	0.083	0.993	0.993	0.100	0.107	0.990	0.989	0.066	0.067	0.996	0.996	
20FL	0.118	0.113	0.986	0.987	0.087	0.090	0.992	0.992	0.071	0.071	0.995	0.995	
30F	0.083	0.083	0.993	0.993	0.074	0.071	0.995	0.995	0.066	0.067	0.996	0.996	
30BL	0.077	0.078	0.994	0.994	0.069	0.072	0.995	0.995	0.063	0.064	0.996	0.996	
30FL	0.085	0.084	0.993	0.993	0.073	0.073	0.995	0.995	0.072	0.072	0.995	0.995	

Table 7 Model performance metrics of aerodynamic moment models around hover

		N	I_x			N	I_y		M_z				
Case	NRMSE		\mathbb{R}^2		NRI	MSE	R	R ²	NRI	MSE	\mathbb{R}^2		
	Full	Test	Full	Test	Full	Test	Full	Test	Full	Test	Full	Test	
Healthy	0.170	0.185	0.971	0.966	0.228	0.230	0.948	0.947	0.603	0.595	0.636	0.646	
10F	0.120	0.122	0.986	0.985	0.137	0.132	0.981	0.983	0.625	0.624	0.610	0.611	
10BL	0.126	0.128	0.984	0.984	0.166	0.168	0.972	0.972	0.620	0.621	0.615	0.614	
10FL	0.156	0.156	0.976	0.976	0.167	0.181	0.972	0.967	0.568	0.567	0.678	0.679	
20F	0.155	0.149	0.976	0.978	0.160	0.154	0.974	0.976	0.691	0.703	0.522	0.505	
20BL	0.208	0.208	0.957	0.957	0.184	0.194	0.966	0.962	0.817	0.728	0.332	0.470	
20BR	0.142	0.141	0.980	0.980	0.190	0.175	0.964	0.969	0.733	0.745	0.463	0.445	
20FL	0.144	0.146	0.979	0.979	0.143	0.146	0.979	0.979	0.663	0.652	0.561	0.574	
30F	0.146	0.145	0.979	0.979	0.180	0.173	0.967	0.970	0.685	0.684	0.53	0.532	
30BL	0.195	0.201	0.962	0.960	0.155	0.160	0.976	0.974	0.747	0.746	0.441	0.444	
30FL	0.185	0.207	0.966	0.957	0.193	0.195	0.963	0.962	0.670	0.671	0.551	0.550	

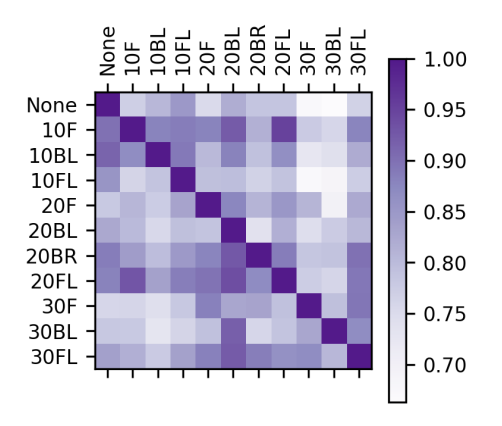
Table 8 Model performance metrics of aerodynamic force models in high-speed flight

		F	7 _x			F	⁷ y		F_z				
Case	NRMSE		\mathbb{R}^2		NRI	MSE	R	22	NRI	MSE	R	R ²	
	Full	Test	Full	Test	Full	Test	Full	Test	Full	Test	Full	Test	
Healthy	0.205	0.206	0.958	0.957	0.137	0.133	0.981	0.982	0.129	0.131	0.983	0.983	
10F	0.252	0.250	0.937	0.937	0.150	0.153	0.978	0.977	0.167	0.164	0.972	0.973	
10BL	0.156	0.155	0.976	0.976	0.194	0.198	0.962	0.961	0.141	0.142	0.980	0.980	
10FL	0.139	0.140	0.981	0.980	0.162	0.166	0.974	0.972	0.130	0.132	0.983	0.983	
20F	0.261	0.260	0.932	0.932	0.140	0.144	0.980	0.979	0.135	0.136	0.982	0.981	
20BL	0.250	0.251	0.937	0.937	0.099	0.093	0.990	0.991	0.139	0.140	0.981	0.980	
20BR	0.219	0.222	0.952	0.951	0.096	0.096	0.991	0.991	0.134	0.134	0.982	0.982	
20FL	0.235	0.236	0.945	0.944	0.198	0.208	0.961	0.957	0.156	0.157	0.976	0.975	
30F	0.247	0.247	0.939	0.939	0.106	0.105	0.989	0.989	0.145	0.144	0.979	0.979	
30BL	0.284	0.283	0.919	0.920	0.122	0.125	0.985	0.984	0.137	0.135	0.981	0.982	
30FL	0.258	0.261	0.934	0.932	0.116	0.117	0.987	0.986	0.145	0.144	0.979	0.979	

Table 9 Model performance metrics of aerodynamic moment models in high-speed flight

		N	I_x			N	I_{y}	
Case	NRI	MSE	R	22	NRI	MSE	R	2
	Full	Test	Full	Test	Full	Test	Full	Test
Healthy	0.124	0.128	0.985	0.984	0.279	0.324	0.922	0.895
10F	0.119	0.121	0.986	0.985	0.270	0.235	0.927	0.945
10BL	0.115	0.114	0.987	0.987	0.435	0.427	0.811	0.818
10FL	0.114	0.114	0.987	0.987	0.250	0.215	0.937	0.954
20F	0.122	0.122	0.985	0.985	0.254	0.253	0.935	0.936
20BL	0.126	0.126	0.984	0.984	0.204	0.206	0.958	0.958
20BR	0.195	0.197	0.962	0.961	0.420	0.431	0.824	0.814
20FL	0.105	0.105	0.989	0.989	0.307	0.285	0.906	0.919
30F	0.217	0.232	0.953	0.946	0.528	0.621	0.721	0.614
30BL	0.237	0.225	0.944	0.949	0.449	0.412	0.798	0.830
30FL	0.136	0.126	0.982	0.984	0.316	0.318	0.900	0.899

these models cannot be directly compared through parameter values as different regressors were chosen between the different models through the SWR algorithm.



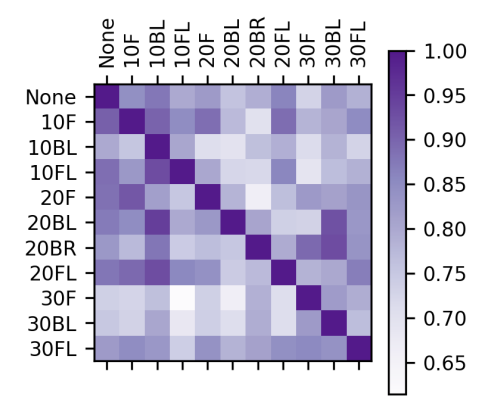


Fig. 9 Element-wise average of model confusion matrices for all low-speed aerodynamic models

Fig. 10 Element-wise average of model confusion matrices for all high-speed aerodynamic models

2. Simplified Fixed-Regressor Models

The simplified models for the low-speed and high-speed flight regimes were built using the regressors listed in Tables 10 and 11 respectively. These regressors were chosen based on the semi-quantitative procedure described in Sec. IV.C. The regressor choices are fairly symmetric for the low-speed case because of the symmetry of the flight maneuvers, evident from the similarities in the F_x and F_y , and F_y , and F_y are F_y and F_y and F_y and F_y and F_y are F_y and F_y are F_y and F_y are F_y and F_y and F_y are F_y are F_y are F_y are F_y are F_y are F_y

Figure 11 shows how the model performance metrics differ between the SWR and FR models, for both speed regimes. Interestingly, the FR models for F_y , F_z , and M_x are virtually as good as the SWR counterparts. The M_y FR models for both airspeed regimes are similarly reduced in accuracy, while for F_x only the high-speed models are significantly worse. These results suggest that the simplification of the models does not significantly reduce the performance of the models. It is again highlighted here that the purpose of the simplifications was to obtain models for different cases with the same set of regressors so that the parameter variations between the damage cases can be compared.

Table 10 Selected regressors for simplified low-speed models Table 11 Selected regressors for simplified high-speed models

Model	Regressors
F_x	$u, \sin(\theta)\omega_{tot}$
F_{y}	$v, \sin(\phi)\omega_{tot}$
F_z	w, ω_{tot}^2
M_{x}	$p, u_p, \cos(\phi)v$
M_{y}	$q, u_q, \cos(\theta)u$
M_z	$r, u_r, \omega_{tot}u_r$

Model	Regressors
$\overline{F_x}$	$u, \sin(\theta)\mu_x, \sin(\theta)u^2$
F_{y}	$v, \sin(\phi)\omega_{tot}$
F_z	w, ω_{tot}^2
$M_{\scriptscriptstyle X}$	$p, u_p, \cos(\phi)v$
M_{y}	q, u_q, μ_z
M_z	-

Figures 12-16 plot the variation of parameter values as a function of blade damage extent and location for the various force and moment models of the low-speed regime. The standard deviations of the parameters are plotted as error bars. It is evident from these plots that, in general, no simple patterns can be found in the parameter values of most of the regressors.

Intuitively, the control moment parameters corresponding to regressors u_p and u_q for the M_x and M_y model respectively are expected to decrease in magnitude with increasing levels of damage. While this is the case for M_x , the decrease in control effectiveness does not follow a logical trend with some model 10% damage showing an increase in

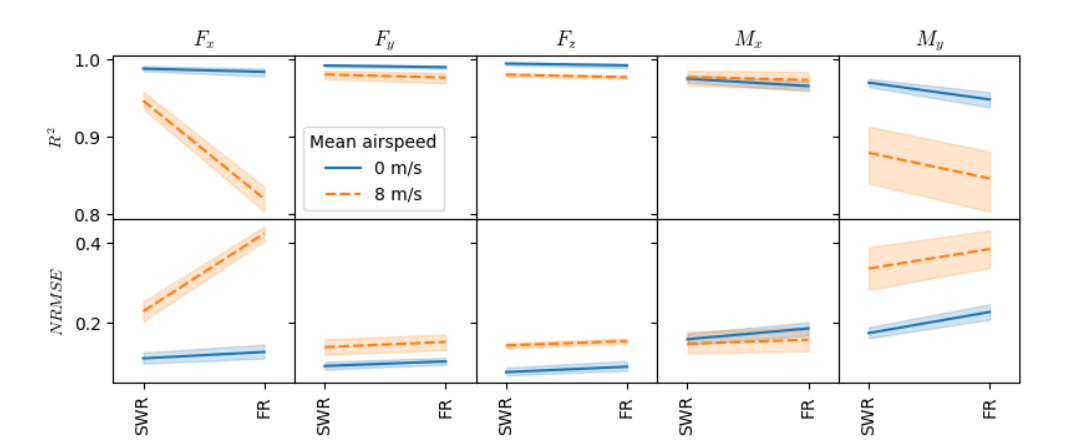


Fig. 11 Model performance metric comparison between the SWR models and the simplified fixed regressor (FR) models

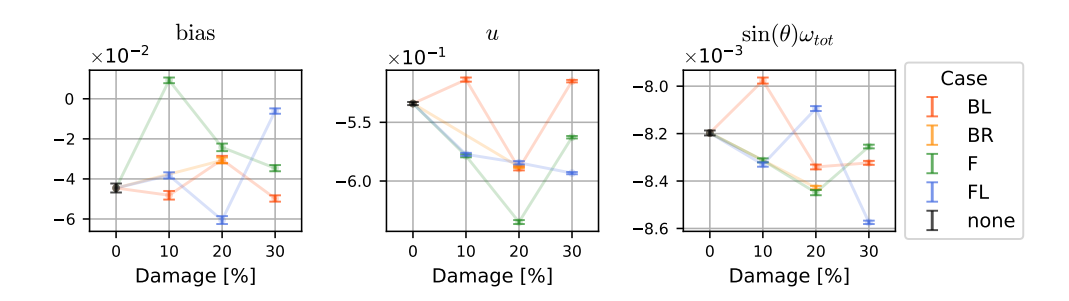


Fig. 12 F_x parameter variations with damage level and location (low-speed regime)

control effectiveness compared to the base models. For example, the control effectiveness remains almost unaffected up to 20% FL damage. The models for M_y on the other hand show an increase in pitch control effectiveness with increasing blade damage which is physically impossible. The bias terms for both M_x and M_y do however show consistent patterns. For example, the M_x bias for F (front) damage stays around the bias corresponding to no damage, which makes sense because the damage is symmetric about the xz plane. The biases for both left-side damage cases –FL and BL– are in agreement, while bias for the BR case seems to be reflected about the zero-damage case bias. Similarly, the bias in M_y is worse for the F damage case compared to the single damage cases, and all the bias decreases or increases in the expected directions in accordance with the location of the damage.

Lastly, the parameters corresponding to the ω_{tot}^2 regressor show a clear pattern with respect to the damage level. There is almost a linear trend, with the F damage case having a higher slope. This makes physical sense, but the question arises why, from the same data, do the control effectiveness parameters not follow meaningful patterns? This is further explored in the next subsection.

The parameters of the high-speed regime models largely show the same non-patterns with respect to blade damage and are therefore omitted for brevity. Interestingly, the M_x models in the high-speed regime reveal clearer patterns in the parameters, as shown in Fig. 17 compared to the low-speed models. The regressor p has the physical interpretation of acting as a damping term. The parameters of this regressor do show a much more prominent pattern than the others (except the bias). Looking at the regressor values, it appears that the roll damping is decreased in the case of front damage, while it is increased in the case of rear damage in the high-speed regime.

The models built by SWR, and therefore the selected regressors are influenced strongly by the system identification maneuvers performed and the regime of airspeeds flown. This is evident by the fact that the regressor $\cos(\theta)u$ selected for the hovering flight was not selected for any of the high-speed models, which apart from being identified at a much higher mean airspeed, also lack the slow speed rolling maneuvers which were performed for the hovering case.

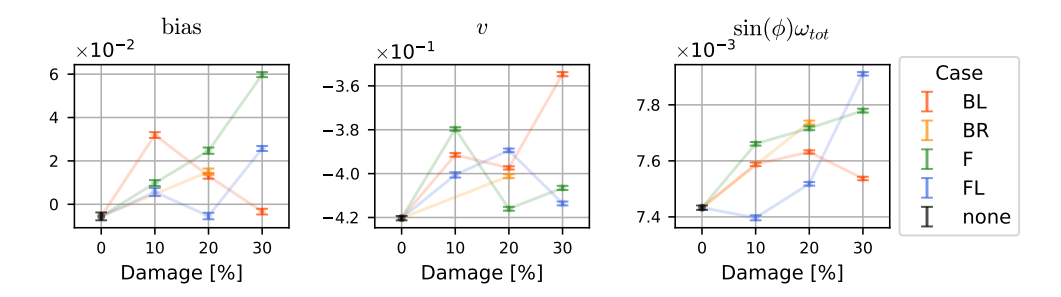


Fig. 13 F_y parameter variations with damage level and location (low-speed regime)

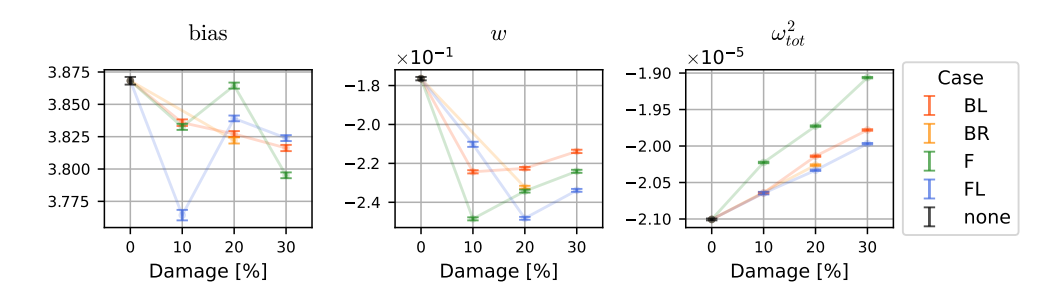


Fig. 14 F_z parameter variations with damage level and location (low-speed regime)

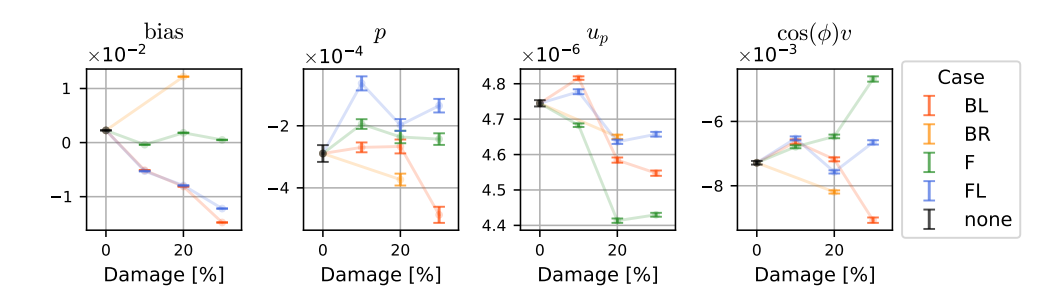


Fig. 15 M_x parameter variations with damage level and location (low-speed regime)

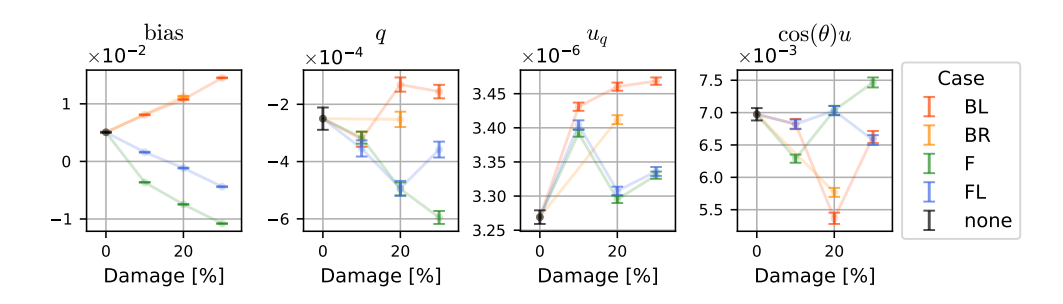


Fig. 16 M_y parameter variations with damage level and location (low-speed regime)

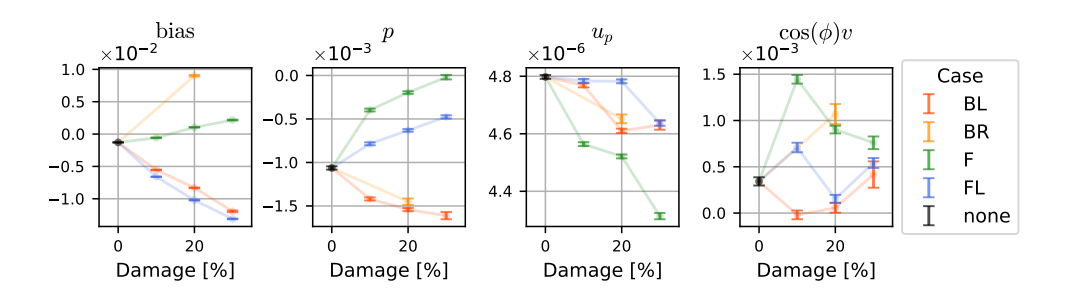


Fig. 17 M_x parameter variations with damage level and location (high-speed regime)

3. Control Effectiveness Analysis

This section tries to uncover the reason for the sporadic estimates of the control effectiveness parameters of the pitching and rolling moments described in the previous subsection. Figures 18 and 19 respectively show the low-speed and high-speed observed forces/moments from training data plotted against the respective primary control effectiveness regressors. Each plot also shows a simple linear model fit to the respective data.

For the F_z model of both speed regimes, a linear trend is clearly observed between F_z and ω_{tot}^2 with decreased slope magnitude at higher damage levels. This is in line with expected behavior; the quadrotor should be less effective in producing thrust when blade damage is present. Conversely, the slope of the (low-speed) M_y model actually increases with increasing damage level, which was also the case for the simplified models shown in Fig. 16.

The low-speed M_x data shows that there are 2 distinct patterns between u_p and M_x . For example, the M_x data shows dominant linear behavior from -0.15 to 0.15 Nm but there is another region with a lower slope, which is active on a smaller range of moment values, roughly -0.03 to 0.03 Nm. This additional non-linear effect was found to occur during the lateral maneuvers while the dominant linear behavior corresponds to the quick roll maneuvers where the lateral airspeed remains close to zero. In the high-speed test flight, only fast roll maneuvers could be performed so as to make sure the quadrotor stays within the jet of the wind tunnel. This is also evident by the fact that the high-speed M_x data shown in Fig. 19 only shows the dominant linear pattern.

Similar to the phenomenon for M_x , similar features can be seen in the M_y data. Unlike the M_x , the pitching moment could be excited both through fast pitch maneuvers as well as slower longitudinal maneuvers during high-speed flight. This is clearly evident in Fig. 19 where two distinct linear regions are visible. The presence of these dual patterns results in the models identified from the data being an unweighted average of both patterns. Since the patterns arise based on the maneuvers performed, differences in flight maneuvers result in different distributions of data for each maneuver which eventually impact the control effectiveness parameters. This would also explain why the high-speed M_x models shown in 17 show clearer patterns than the other models, only one type of maneuver was flown for this case.

These findings suggest that linear-in-the-parameters models may not be sufficient to model the dynamics of a quadrotor from a physical perspective. For example, the roll control effectiveness is found to depend on additional states such as lateral airspeed in a non-linear fashion, while also of course depending on the control input created by the combination of rotor speeds.

B. High-Frequency Models

1. Spectral Analysis

While the simplex B-spline models are the primary result of the HF models, the frequency-amplitude data gathered from the spectral analysis of the raw IMU data is interesting to analyze. Here, the results obtained for a variety of damage cases for both the Beetle and Geyser drones are presented. First, the results for a single damage case are presented which show the amplitude-frequency relationships of three harmonics for each IMU axis. Then, similar plots are shown for increasing levels of damage at a single location. Finally, results are shown for the same damage level at all four damage locations.

Figures 20 and 21 show the f - A relationships as mean value (solid lines) and 2σ bands (shaded regions) for the Beetle and Geyser quadrotors respectively. These results are obtained from a single flight with a duration of around 120 seconds. The duration of flights for the remainder of the HF spectral analysis results are derived from flights of similar

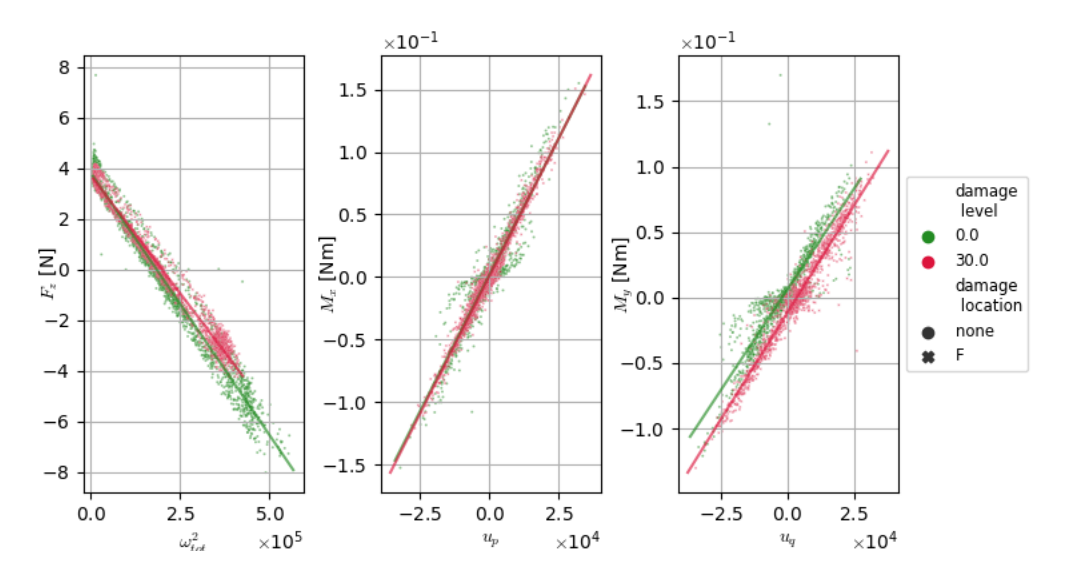


Fig. 18 Control effectiveness comparison plots for low-speed flight data

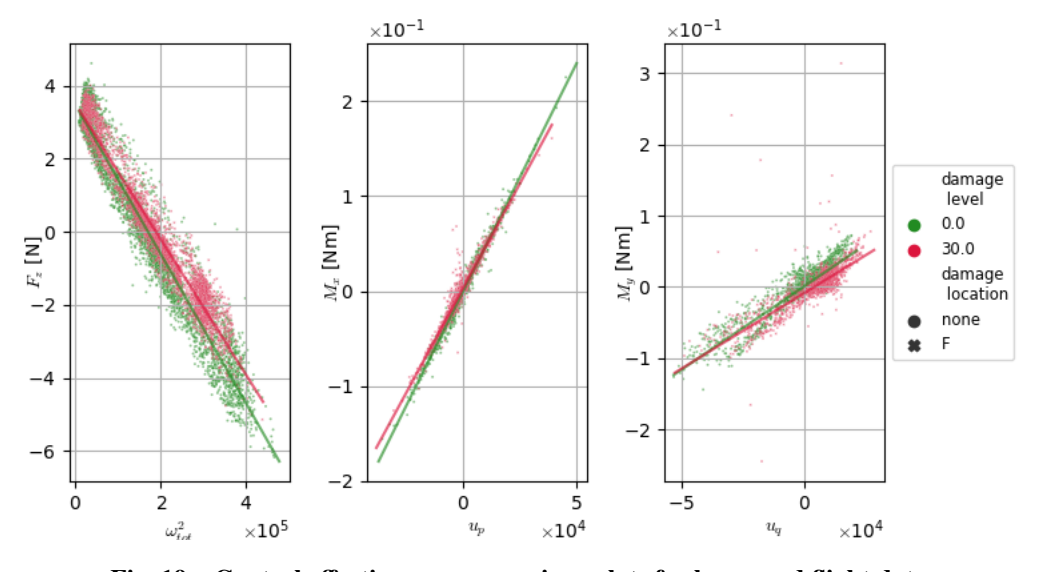


Fig. 19 Control effectiveness comparison plots for low-speed flight data

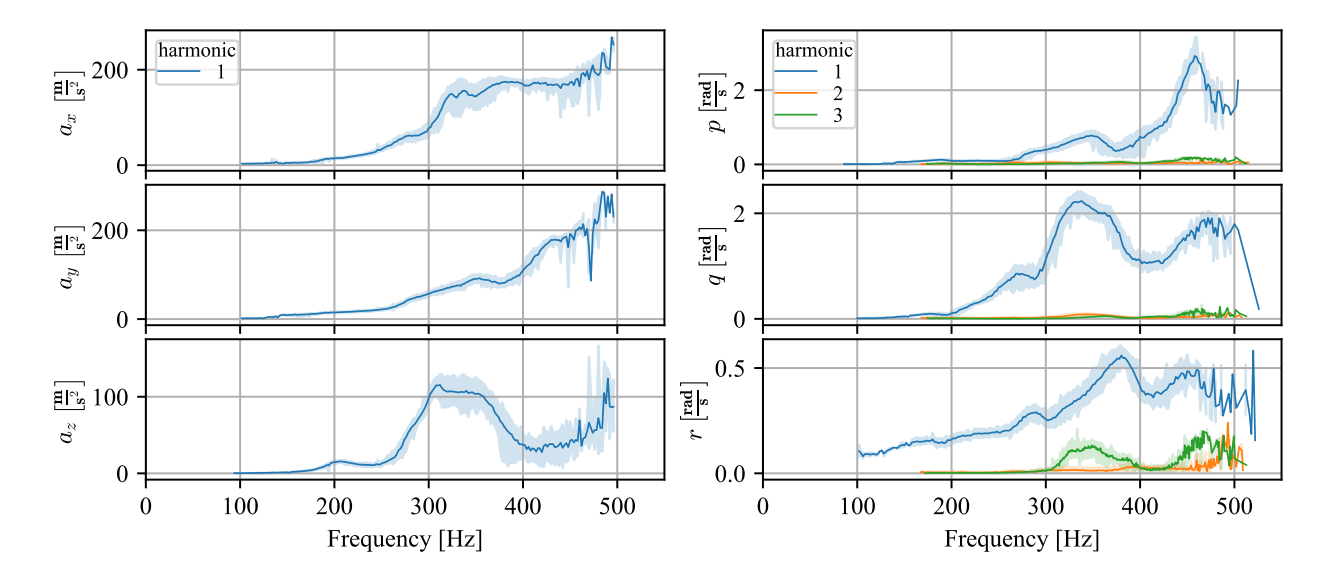


Fig. 20 Amplitude-frequency relationships of the Beetle quadrotor with damage case 30FR

duration.

Since the accelerometer on the Beetle is sampled at 1000 Hz, only the first harmonic is extracted. Another important point to note is that the accelerometers of both quadrotors have a limit of 16 g (160 m/s), yet the estimated amplitudes tend to surpass this value for the Beetle. This occurs at frequencies close to the Nyquist limit (500 Hz), where the STFT does start to break down given the very short time windows. This is an inherent limitation and requires the use of IMUs with higher sampling rates and higher saturation limits. Additionally, as mentioned in Sec. IV.B, high frequencies are difficult to excite in an indoor environment, which results in fewer data points in these regions, accounting partly for the noisy data at frequencies above 450 Hz.

Figure 21 shows that the high-frequency region (>450 Hz) for the Geyser drone is less noisy than the Beetle. Unlike the Beetle, the accelerometer of the Geyser has a logging rate of 8 kHz. Additionally, the higher mass of the Geyser results in higher hovering RPM, making the full range of frequencies easier to cover through throttle punch maneuvers. The higher inertia of the Geyser also makes the accelerometer less susceptible to clipping.

It is interesting to note that the harmonics above the base harmonic have a relatively small contribution to the time-series signal. For the Beetle, the higher harmonics only contribute significantly to the yaw rate, while the Geyser has the highest contributions in a_z with noticeable peaks around 300 Hz for the other IMU measurements.

Figure 22 shows that increasing levels of blade damage manifest in clear differences between the f-A relationships for all the IMU axes of the Beetle quadrotor. Figure Figure 24 also shows that the location of damage results in different f-A relationships at the same damage level. In both the figures, there are multiple lines of the same color which signifies data obtained from completely separate flights with the same damage case, which shows the reproducibility of the results obtained from the spectral analysis procedure explained in Sec. IV.D. It is interesting to see that the curves at different damage levels show similar localized features which increase in prominence as the damage level increases. These effects are likely caused by structural resonance in the airframe and complex aerodynamic interactions.

Figure 23 and 25 show the same effects seen from the corresponding plots for the Beetle quadrotor on the Geyser quadrotor. However, the mean f - A curves appear to be noisier for the Geyser, with larger 2σ bands. After a closer inspection of the raw IMU data, and the frequency and amplitude estimates at each time point, it was found that there may be a dependence of amplitude on additional states apart from f. For example, Fig. 26 shows the roll-rate data of the Geyser with damage case 30FR. A clear oscillation in the amplitude of the signal is seen which at first looks independent of the frequency of the signal, but there is a pattern visible of lower amplitudes corresponding to lower frequencies and vice-versa. This oscillation in frequency is also weakly visible in the STFT plot. These oscillations in amplitude were also observed on the Beetle but to a much lower extent.

There are two explanations for the high-frequency amplitude oscillation phenomenon. For one, the assumption that the amplitude is only a function of frequency may still be valid. This suggests that the high-frequency oscillations in

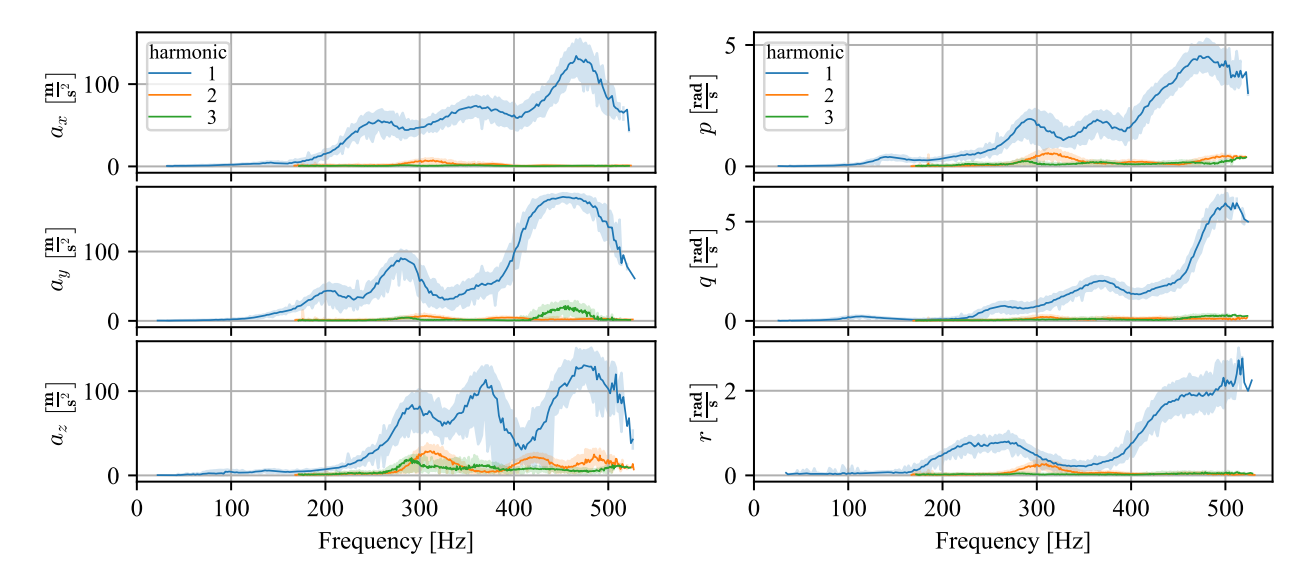


Fig. 21 Amplitude-frequency relationships of the Geyser quadrotor with damage case 30FR

frequency are caused by fast oscillation in motor RPM values, and the amplitude is directly related to these frequency oscillations. However, it is difficult to resolve these dynamics with the STFT because the frequency changes very rapidly. This essentially means that the signal is too non-stationary to capture the frequency and amplitude by analyzing even small time windows. This is also visible in Fig. 26, where the estimated amplitude does not perfectly conform to the signal.

Alternatively, there may be hidden states governing this oscillation in signal amplitude. It is important to note that the flight controller on the Geyser drone is mounted on the airframe via rubber standoffs which include metal inserts for securing the board with fasteners. The Beetle on the other hand has steel standoffs that are many orders of magnitude stiffer. It is possible that the high levels of vibration cause non-linear structural effects through the rubber standoffs which do not occur with the same severity on the Beetle. In either case, even though the high-frequency amplitude and frequency oscillation of the signal cannot be resolved, the mean f - A relations are still captured.

2. Simplex B-spline Models

The surfaces of the simplex B-spline models constructed for the Beetle quadrotor of the amplitudes corresponding to the first harmonic, for the FR damage case, are presented in Fig. 27. The training data is also shown in these plots but reduced to the mean value at each frequency bin for each damage level. The spline surfaces go through the training data and are able to capture all the local non-linearities in the data. Additionally, the regions in between the rows of training data appear to be qualitatively well interpolated by the spline models. The models for the second harmonic are shown in Fig. 28. The training data appears nosier in this case but it is also important to notice that the amplitudes of the second harmonic are much lower in value than that of the first harmonic. The training data is especially noisy in the low and high-frequency regions. The noise in the low-frequency region is likely caused by leakage of amplitudes estimated for the first harmonic into the second harmonic, while noise in the high-frequency regions is likely because of fewer data points in each frequency bin as explained in the previous section.

The performance metrics for the various simplex B-spline models of the Beetle quadrotor are summarised in Table 12 and Table 13 for the accelerometer and gyroscope models respectively. The results are shown calculated on the entire dataset (*Full*) as well as the validation set (*Test*). The data was split randomly into the 80:20 ratio for the training and validation sets for all the models. Note that because the MPU6000 IMU is limited to 1 kHz, only the first harmonic models are possible to construct for the Beetle.

From the results, some general conclusions can be drawn. The base harmonic models generally perform significantly better than those corresponding to higher harmonics. Since the base harmonic is the dominant component, this is not a very consequential limitation. The performance metrics for the validation data are comparable to those of the complete dataset, which indicates that the models do not overfit the training data.

It is interesting to note the BL accelerometer models show worse performance than the other damaged locations.

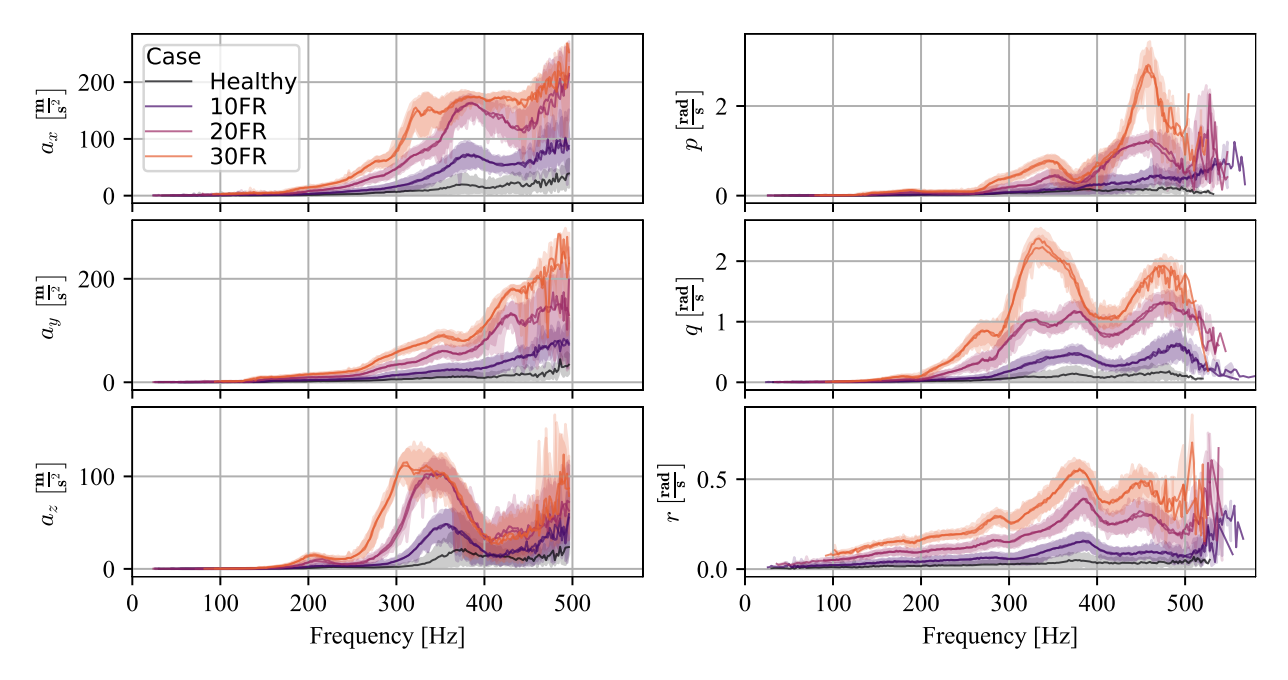


Fig. 22 Amplitude-frequency relationships of the first harmonic at varying levels of FR damage for the Beetle

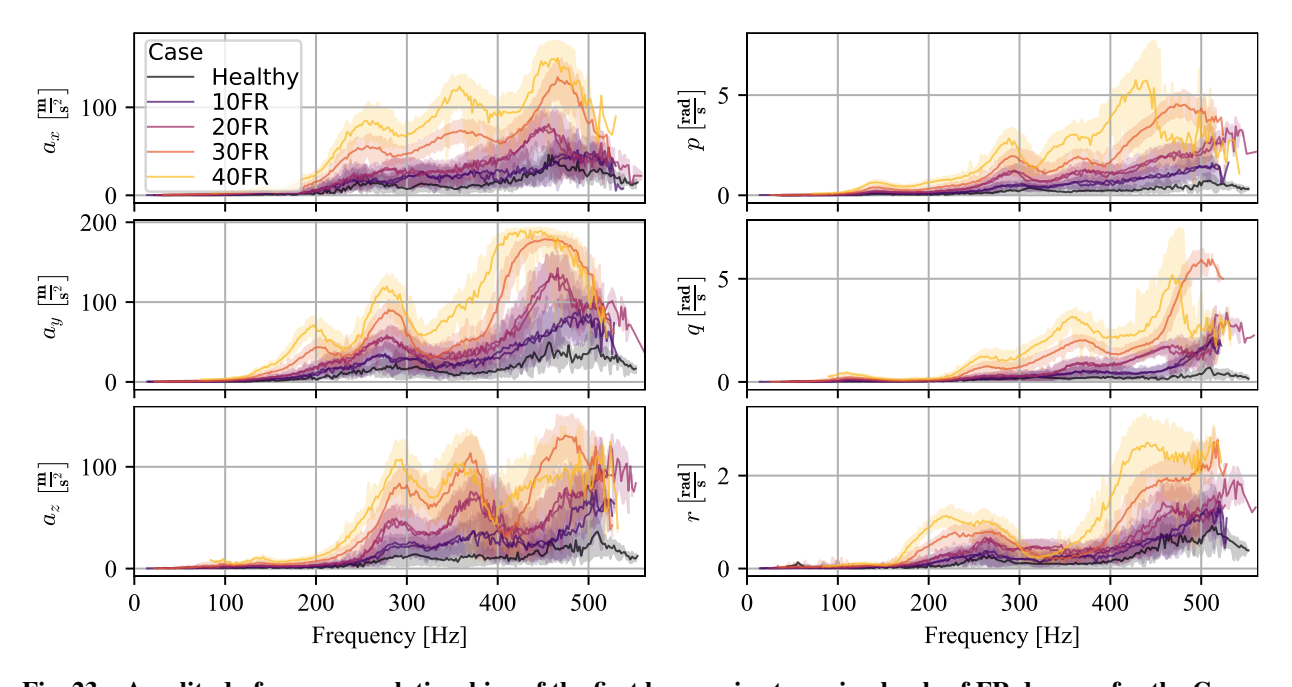
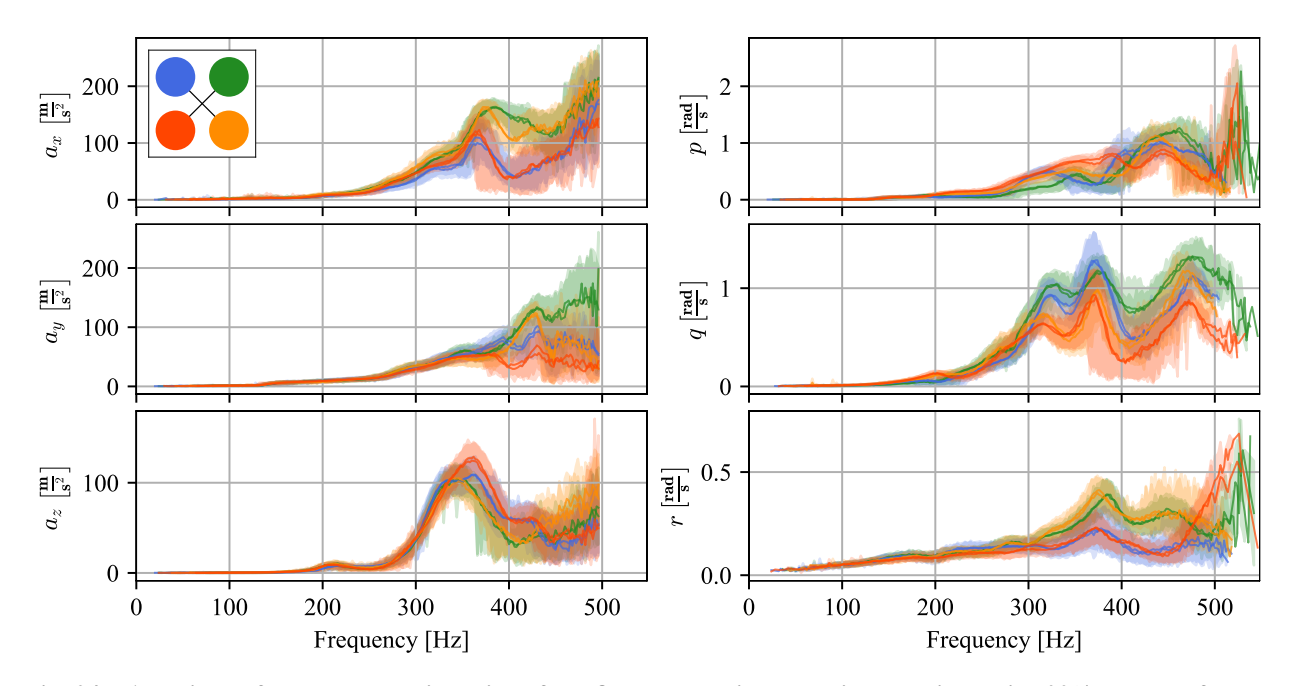
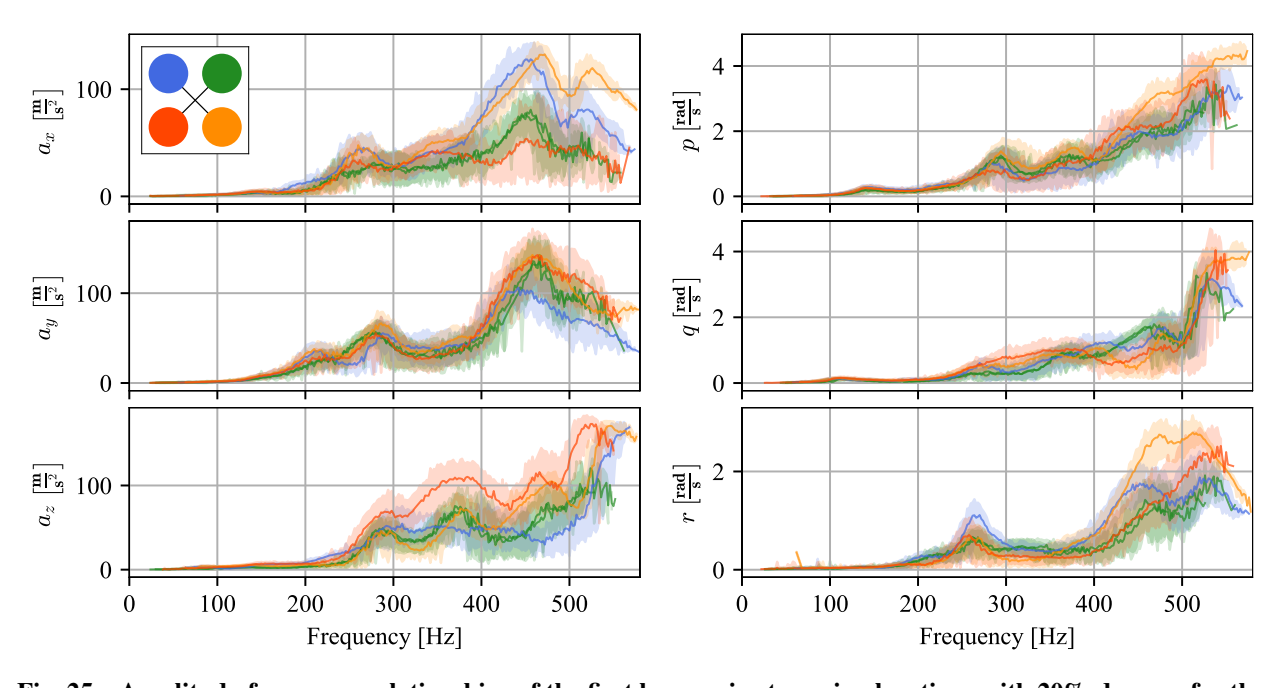


Fig. 23 Amplitude-frequency relationships of the first harmonic at varying levels of FR damage for the Geyser



 $Fig.~24 \quad Amplitude-frequency~relationships~of~the~first~harmonic~at~varying~locations~with~20\%~damage~for~the~Beetle$



 $Fig. \ 25 \quad Amplitude-frequency \ relationships \ of the \ first \ harmonic \ at \ varying \ locations \ with \ 20\% \ damage \ for \ the \ Geyser$

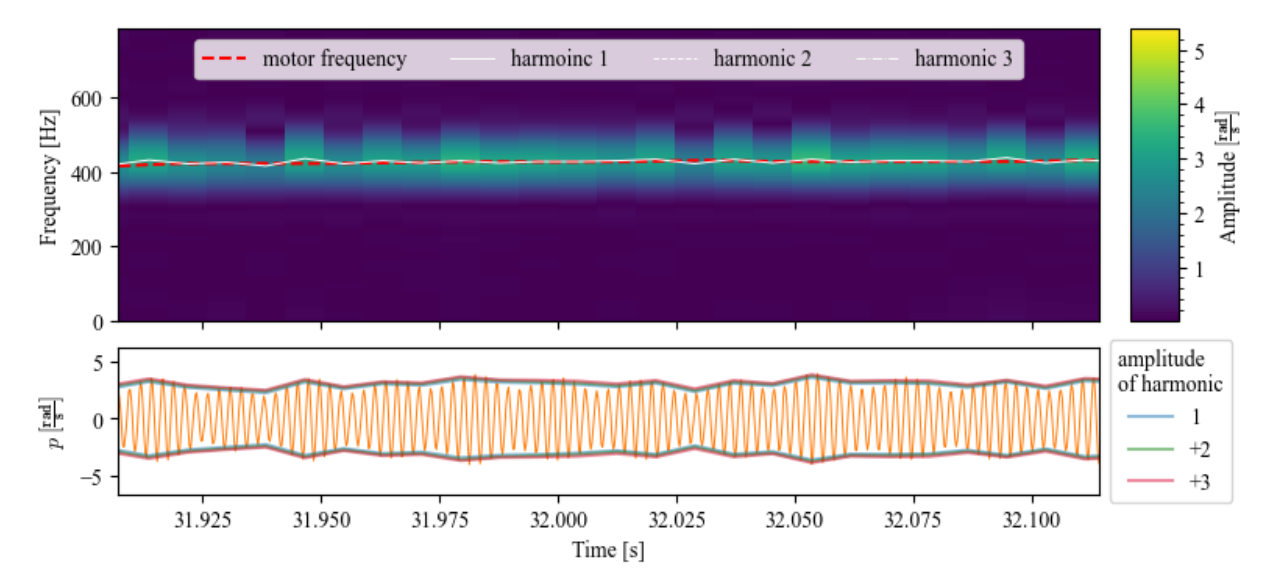


Fig. 26 A time-snippet of the roll rate (bottom) measured by the Geyser quadrotor for damage case 30FR, and the spectrogram of this signal showing peak harmonics related to the motor frequency (top)

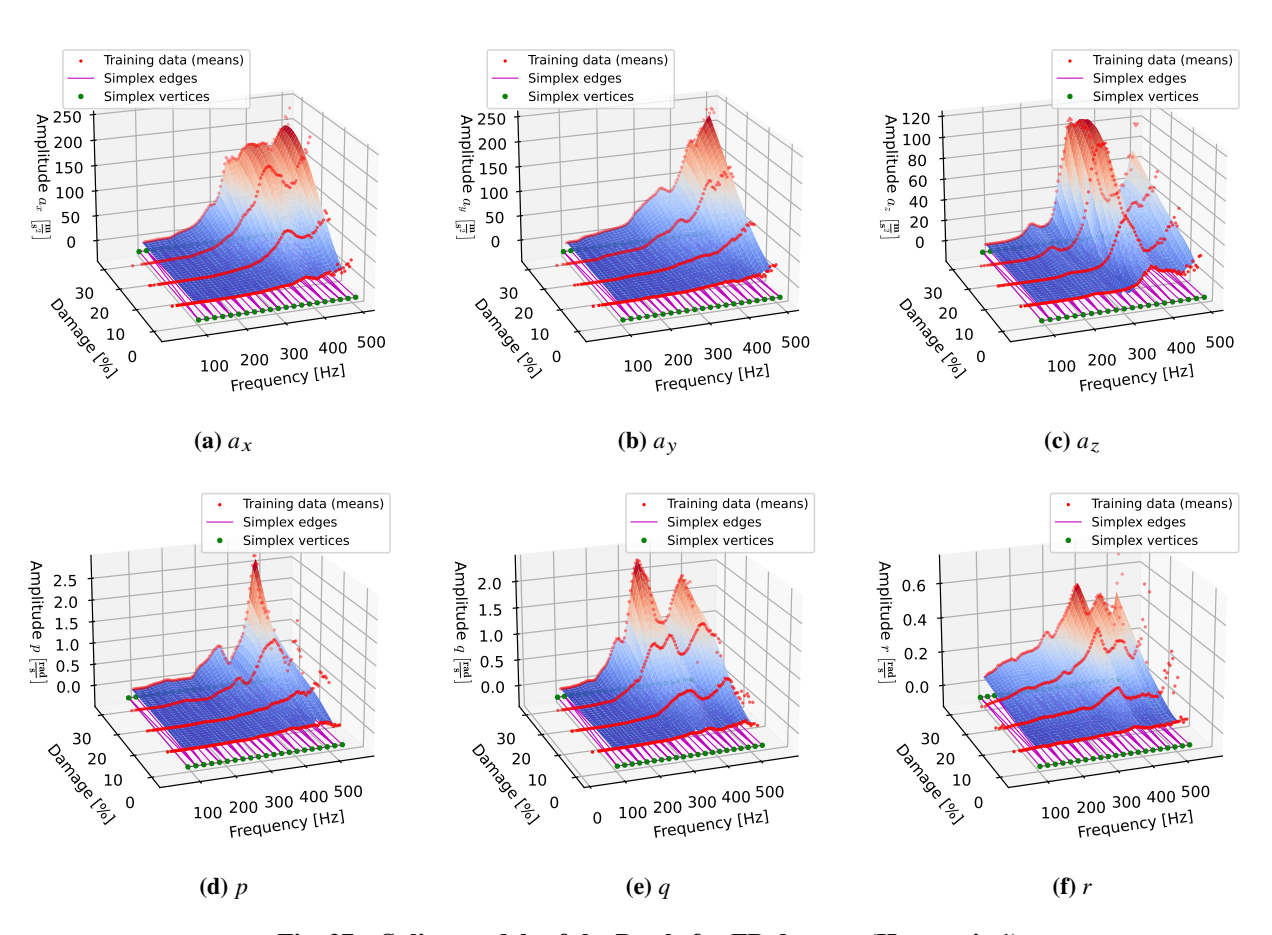


Fig. 27 Spline models of the Beetle for FR damage (Harmonic 1)

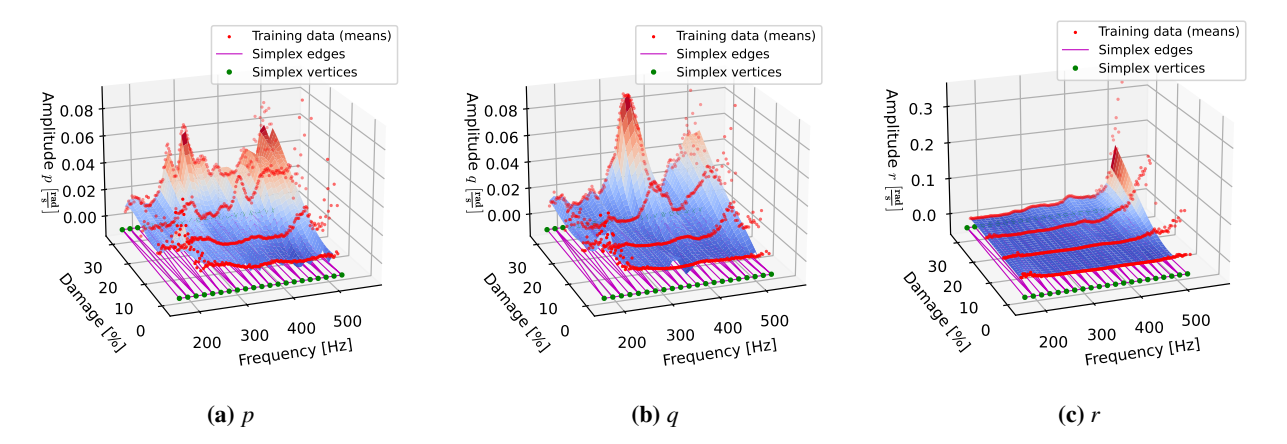


Fig. 28 Spline models of the Beetle for FR damage (Harmonic 2)

Table 12 Model performance metrics for the HF acceleration models of the Beetle quadrotor (h = harmonic)

			а	x			а	y		a_z				
Case	Case h		NRMSE		\mathbb{R}^2		NRMSE		\mathbb{R}^2		MSE	R ²		
		Full	Test	Full	Test	Full	Test	Full	Test	Full	Test	Full	Test	
FR	1	0.171	0.173	0.971	0.970	0.194	0.191	0.963	0.964	0.239	0.241	0.943	0.942	
FL	1	0.285	0.292	0.919	0.915	0.200	0.201	0.960	0.960	0.223	0.219	0.950	0.952	
BR	1	0.174	0.173	0.969	0.970	0.220	0.222	0.952	0.951	0.147	0.147	0.979	0.979	
BL	1	0.323	0.323	0.895	0.896	0.309	0.302	0.905	0.909	0.189	0.186	0.964	0.966	

Looking at the top row of plots in Fig. 29, it appears that noise in the high-frequency regions (>450 Hz) is the probable cause. The noisy data in the high-frequency region are likely present because of the proximity of these frequencies to the Nyquist limit (500 Hz). The gyroscope models for the BL case are not always worse than the other damage locations. The gyroscope data is sampled at 8 kHz, which further suggests that accelerometer model training data is inflicted with noisy estimates due to proximity to the Nyquist limit.

The performance metrics for the simplex B-spline models of the Geyser quadrotor are summarised in Table 14 and Table 15 for the accelerometer and gyroscope models respectively. Unlike the Beetle, the 8 kHz sampling rate of the accelerometer in the ICM42605 IMU facilitates the identification of accelerometer models at harmonics higher than the base harmonic. Note that models only for the FR location are presented even though Table 4 suggests that all 4 single-damage locations were tested. This is because apart from the FR case, the other cases only cover one damage level, to qualitatively analyze how the f - A relationships change based on damage location, at the same damage level, for the Geyser quadrotor.

On average, the base harmonic models of the Geyser seem to be slightly worse than the Beetle. This is likely because of the high-frequency amplitude oscillation phenomenon described in the previous section. The models of the higher harmonics also show significantly worse performance than those of the base harmonics, as was the case with the Beetle.

In addition to creating models for the damage levels for which flight data was gathered, the simplex B-spline models also facilitate interpolation between the damage levels. To examine how accurately the spline models are capable of interpolating between damage levels, flight data was gathered for two damage cases: 15BL and 25FL (see Table 3). The data for these cases were not used to construct the models for the respective damage locations.

Figure 29 shows plots of the training data, spline models, and validation data for the BL damage case of the Beetle quadrotor. The validation data corresponds to a damage level of 15% and was not used when identifying the simplex B-spline model. It can be seen from the plot of each model in Fig. 29 that the spline model is actually able to approximate the data obtained for the 15% damage case quite well for all six models, even capturing the local peaks and valleys as a function of frequency.

Table 13 Model performance metrics for the HF angular-rate models of the Beetle quadrotor (h = harmonic)

			1	p			Ç	7		r				
Case	h	NRI	MSE	R	22	NRI	MSE	R	22	NRI	MSE	R	22	
		Full	Test											
	1	0.243	0.236	0.941	0.945	0.137	0.134	0.981	0.982	0.180	0.179	0.967	0.968	
FR	2	0.525	0.536	0.724	0.712	0.38	0.398	0.855	0.841	0.457	0.475	0.771	0.759	
	3	0.318	0.317	0.893	0.894	0.391	0.402	0.815	0.819	0.349	0.352	0.877	0.875	
	1	0.253	0.250	0.936	0.937	0.169	0.168	0.971	0.972	0.365	0.367	0.867	0.866	
FL	2	0.495	0.482	0.755	0.767	0.532	0.513	0.718	0.737	0.462	0.464	0.784	0.781	
	3	0.367	0.368	0.864	0.863	0.389	0.387	0.816	0.815	0.322	0.323	0.882	0.882	
	1	0.217	0.218	0.953	0.953	0.206	0.204	0.958	0.958	0.176	0.176	0.969	0.969	
BR	2	0.286	0.288	0.920	0.918	0.625	0.620	0.615	0.622	0.509	0.519	0.591	0.583	
	3	0.274	0.272	0.912	0.913	0.172	0.163	0.895	0.896	0.258	0.262	0.929	0.928	
	1	0.209	0.216	0.956	0.953	0.288	0.287	0.917	0.918	0.305	0.299	0.905	0.909	
BL	2	0.455	0.403	0.791	0.837	0.634	0.634	0.594	0.594	0.491	0.470	0.747	0.764	
	3	0.268	0.271	0.925	0.924	0.245	0.237	0.934	0.937	0.275	0.279	0.924	0.922	

Table 14 Model performance metrics for the HF acceleration models of the Geyser quadrotor (h = harmonic)

			а	x			а	y		a_z				
Case	h	NRMSE		\mathbb{R}^2		NRMSE		R	22	NRMSE		\mathbb{R}^2		
		Full	Test	Full	Test	Full	Test	Full	Test	Full	Test	Full	Test	
	1	0.236	0.233	0.945	0.946	0.204	0.210	0.958	0.956	0.336	0.341	0.887	0.884	
FR	2	0.327	0.357	0.893	0.873	0.355	0.348	0.874	0.879	0.28	0.29	0.922	0.916	
	3	0.717	0.723	0.488	0.479	0.359	0.363	0.872	0.870	0.494	0.49	0.756	0.761	

Table 15 Model performance metrics for the HF angular-rate models of the Geyser quadrotor (h = harmonic)

			1	p			Ç	7		r				
Case	h	NRMSE		\mathbb{R}^2		NRI	NRMSE		\mathbb{R}^2	NRI	MSE	R	\mathbb{R}^2	
		Full	Test	Full	Test	Full	Test	Full	Test	Full	Test	Full	Test	
	1	0.262	0.270	0.932	0.928	0.233	0.226	0.947	0.950	0.260	0.259	0.934	0.934	
FR	2	0.334	0.320	0.889	0.898	0.385	0.424	0.852	0.821	0.313	0.320	0.902	0.898	
	3	0.509	0.514	0.740	0.735	0.515	0.535	0.736	0.714	0.640	0.658	0.590	0.567	

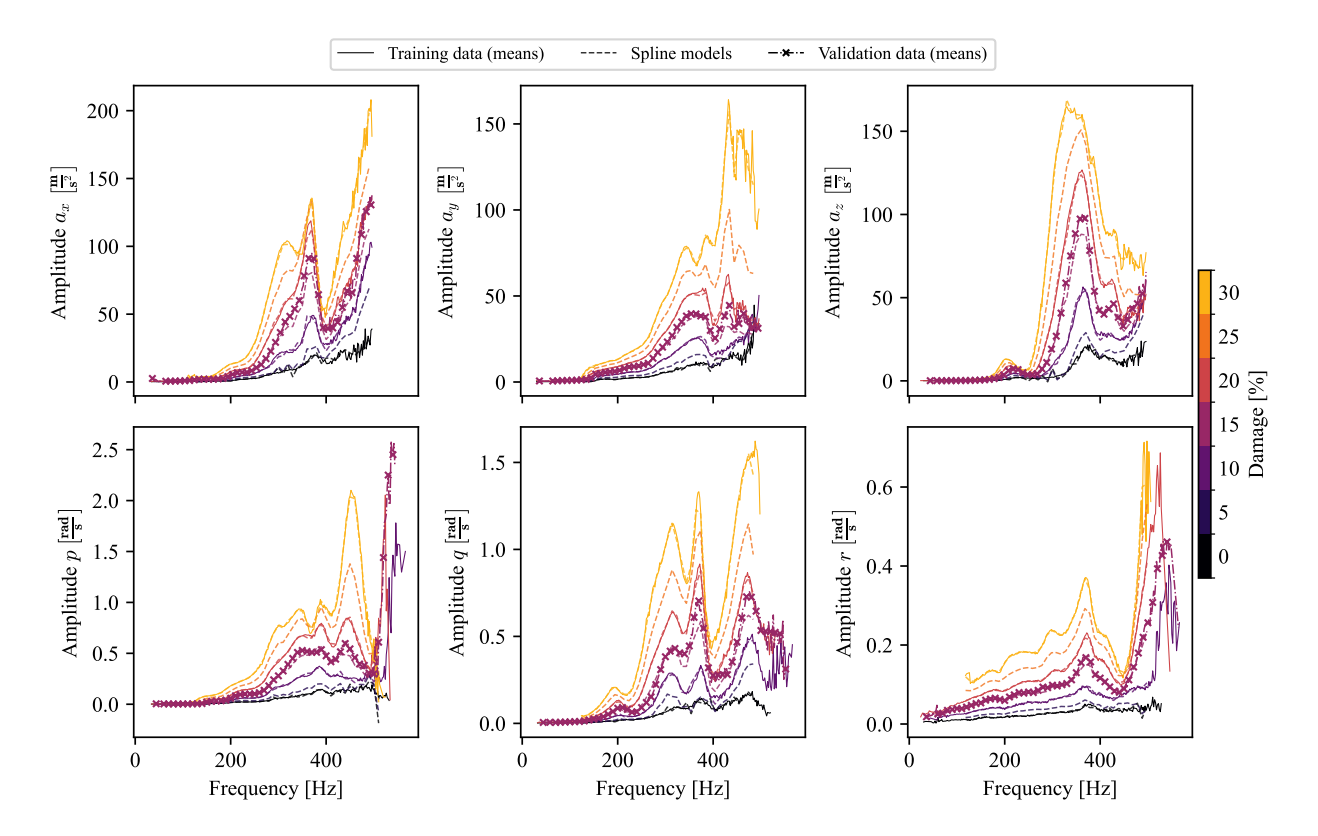


Fig. 29 Projected spline models of the Beetle for BL damage (Harmonic 1)

Table 16 Interpolation performance of the HF acceleration models

Case	h	a_x		a_y		a_z	
		NRMSE	R ²	NRMSE	R ²	NRMSE	R ²
15B1	1	0.475	0.774	0.516	0.734	0.291	0.915
25FL	1	0.339	0.885	0.323	0.895	0.297	0.912

Figure 30 shows similar plots as Fig. 29, but for FL damage, with validation data recorded at 25% damage. Again, the spline models are able to interpolate the 25% damage case quite well. However, roll rate (p) and a_y models perform relatively poorly at the higher frequency region. Models for q and r are particularly accurate.

Tables 16 and 17 respectively show the model performance metrics for the accelerometer and gyroscope models at both interpolated damage cases. While the error for the interpolated damage levels is higher than that of the damage levels used for training the model, the models still give a decent approximation. This shows the feasibility of simulating the HF behavior at several damage levels with HF models built from a discrete set of a few damage levels, which is a novel finding of this research.

VI. Discussion

A. Aerodynamic Models

While the aerodynamics models identified through SWR show good performance and are able to capture the effects of different combinations of blade damage and extent, they do not offer a meaningful method of interpolating between damage levels at a given damage case because of the differences in regressors chosen from one damage case to the next. The simplified fixed-regressor models identified to remedy this also did not show many meaningful relationships in the

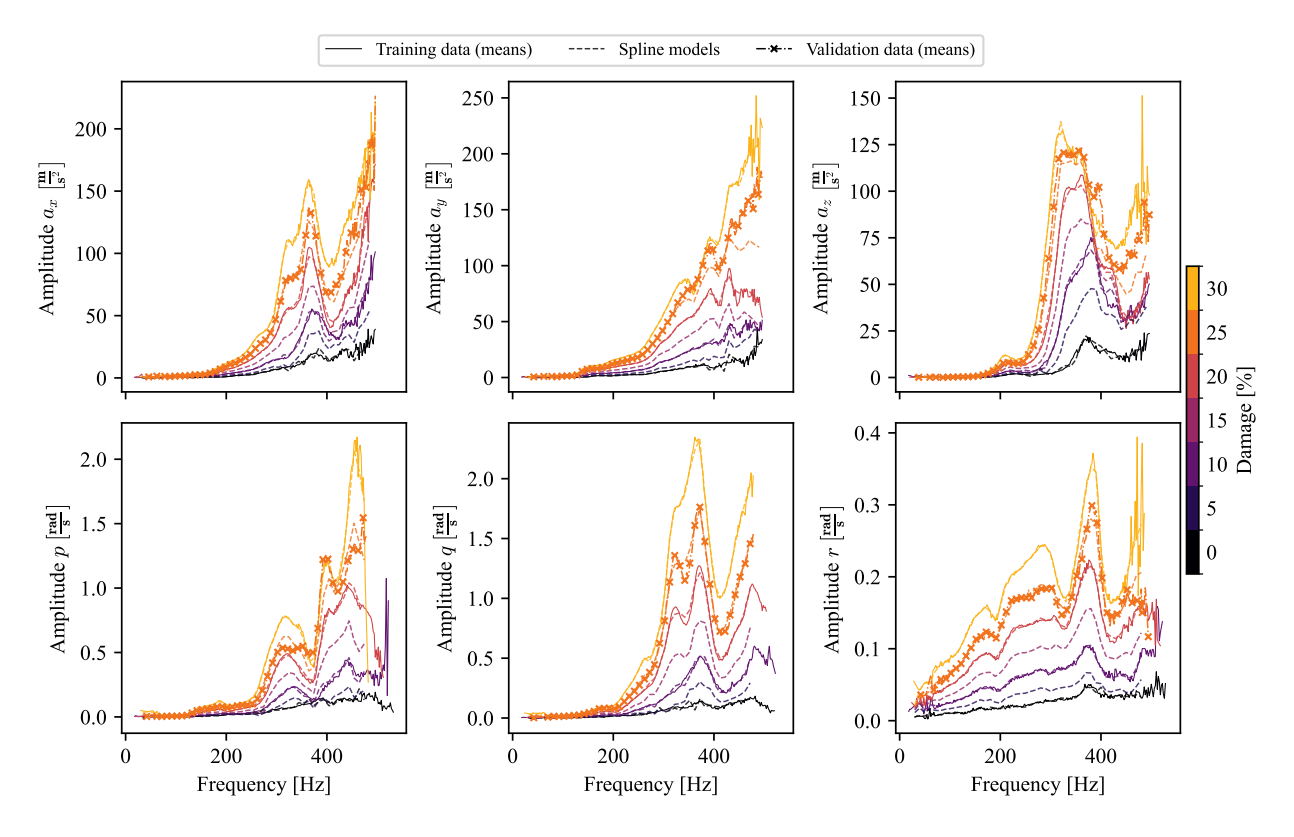


Fig. 30 Projected spline models of the Beetle for FL damage (Harmonic 1)

Table 17 Interpolation performance of the HF angular-rate models

Case	h	p		q		r	
		NRMSE	R ²	NRMSE	R ²	NRMSE	R ²
15BL	1	0.411	0.831	0.547	0.701	0.602	0.638
	2	0.911	0.171	0.999	0.002	0.600	0.640
	3	0.330	0.891	0.248	0.938	0.345	0.881
25FL	1	0.320	0.897	0.231	0.947	0.572	0.672
	2	0.581	0.662	0.619	0.617	0.474	0.776
	3	0.377	0.858	0.661	0.564	0.483	0.767

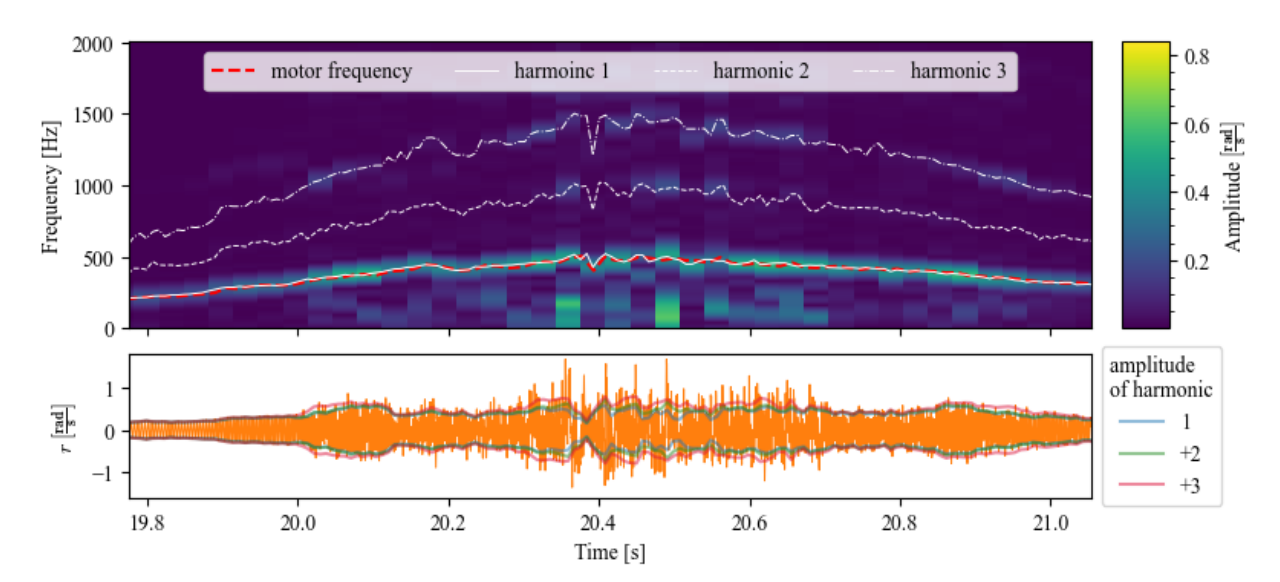


Fig. 31 A time-snippet of the yaw rate (bottom) measured by the Beetle quadrotor for damage case 30FR, and the spectrogram of this signal showing peak harmonics related to the motor frequency (top)

parameter values as a function of blade damage location and level. Exceptions to this were the ω_{tot}^2 regressor parameters of the F_z models, and the biases of the M_x and M_y models. However, it must be noted that the bias component of the moment models merely accounts for the constant offsets in rotor speeds created due to blade damage, and does not model the actual moments produced when maneuvers are performed.

One major reason for the lack of meaningful variations in model parameters as a function of blade damage was that, depending on the flight maneuvers performed, the training data can significantly impact the identified model parameters. Even though the system identification flights were performed manually, the variation between the maneuvers between flights was tried to be kept at a minimum by following a fixed set of pre-planned maneuvers. However, this clearly did not prove to be enough, suggesting that the only way to ensure that flight maneuvers are performed in a repeatable manner is to perform automated test flights, where pose feedback information provided by an external motion capture system is used to control the attitude and position of a quadrotor. This has been done by Sun et al. [31]. The automation of flight should also allow for more complicated maneuvers to be flown which better couple the forces and moments, unlike the largely uncoupled models presented in this paper.

The analysis of the control effectiveness regressors described in Sec. V.A also shows the difficulty of capturing meaningful physical relationships using linear-in-the-parameters polynomial models. This was especially evident for the moment control effectiveness regressors u_p and u_q for the M_x and M_y models respectively.

B. High Frequency Models

One of the base assumptions used when building the HF models is that high-frequency accelerations and angular rates measured in each axis are comprised of a few sinusoids. Specifically, we further assume that the dominant sinusoid has a frequency equal to the rotation frequency of the damaged propeller, and only the harmonics of this frequency are dominant. While this was found to be the case for almost all IMU measurements of both the Beetle and Geyser, the yaw rate measured on the Beetle shows additional oscillations at sporadic frequencies below the motor frequency shown in Fig. 31. This generally occurs above around 250 Hz but is most dominant at frequencies above 400 Hz. The limitation of the HF modeling approach is that these sporadic effects are not captured.

While the spline-based HF models show the possibility of predicting signal amplitudes at damage levels in between the levels corresponding to the training data, a spacing of 10% damage between the training data may be too high to accurately reproduce the behavior in between the training damage levels. The spacing between damage levels also affects the number of test flights required, so a trade-off is required in terms of accuracy and experimental costs.

The phase relationships between the harmonics of each IMU axis, as well as the phase relationships between these

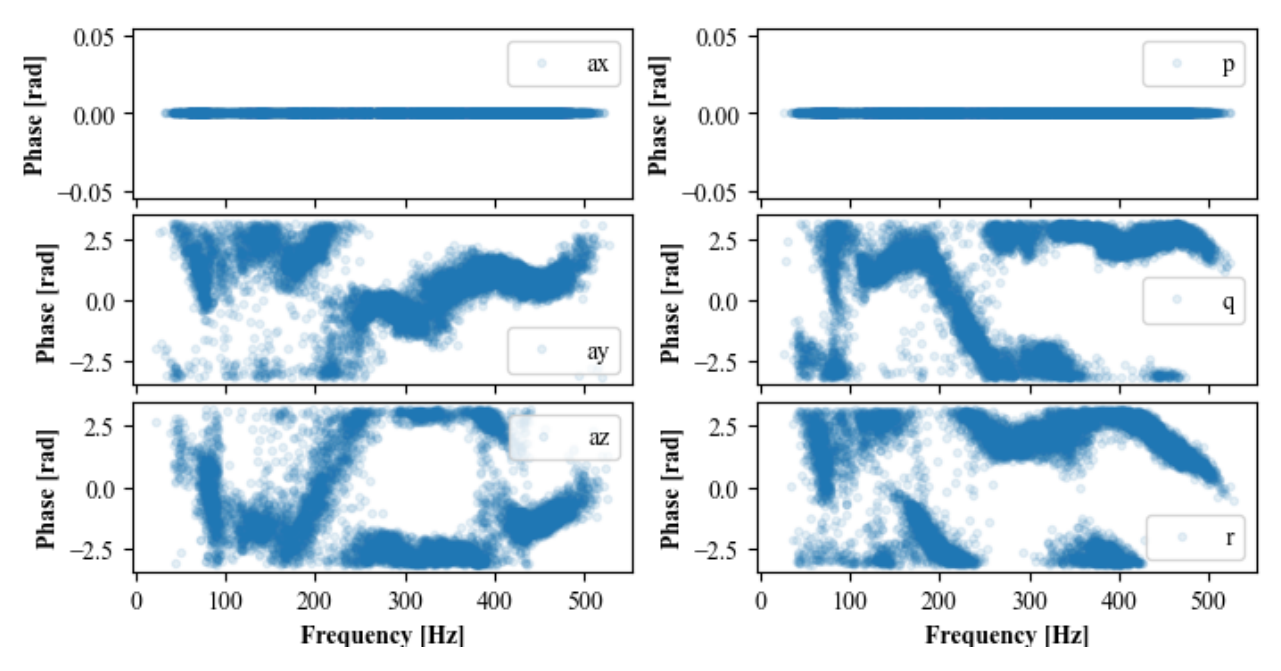


Fig. 32 Relative phases of the IMU signals of the Geyser, with damage case 30FR, obtained from the STFT of each respective signal.

axes, are not described by the HF models presented in this paper. This would be a useful addition, whereby phase relationships are constructed as a function of frequency in a similar manner as was done for the amplitudes in this paper. Figure 32 shows the phase information extracted from the 30FR damage case of the Geyser. Since the absolute phase depends on the actual angle made by the damaged rotor with respect to a fixed body reference – an unmeasured quantity—it is impossible to obtain the absolute phase of each IMU signal. However, at each slice of the STFT, the relative phases between signals can be computed. In Fig. 32, the phase of a_y and a_z is shown relative to that of a_x , while the phases of a_y and a_z are shown relative to that of a_z . Interestingly, there are clear patterns visible in the phase data as a function of frequency. However, the phase data obtained for damage levels below 30% are not as clear as shown here, and almost look random at 10% damage even though the IMU signals are sinusoidal for all damage cases. Therefore, before phase models can be constructed, accurate extraction of phase information should be investigated.

The simplex B-spline models presented in this paper use a fairly simple triangulation which is defined on a rectangular grid of points. To better cover the complete data space, the convex hull of the data should be used to select the simplex vertices. In terms of the number of simplices in each direction, the triangulation presented here shows good results and is recommended to be kept the same for amplitude surface modeling.

The HF models treat frequency as the only independent variable (at a constant damage level). However, there may be a weak dependence on additional variables that affect the aerodynamic imbalances created by the damaged propeller. For example, the angle of attack of the rotor plane and airspeed may increase or decrease the effects of the HF forces and moments caused by aerodynamic imbalances which are not accounted for in the presented models. A few HF model identification flights were also conducted in the wind tunnel to see the effects of mean flow velocity on the frequency amplitude curves obtained from spectral analysis. Figure 33 shows the amplitude-frequency relationship for the same damage case, but flying at different mean airspeed. Note that the multiple curves for the '0 m/s' case each correspond to a unique flight. From these results, it is clear that frequency-amplitude relationships do not change drastically at different air speeds.

It is important to note here that the variations between the green curves (all corresponding to the same damage case) in Fig. 33 seem quite large compared to what was shown in Fig. 20 for various damage cases. This is likely because of minor changes in mass, and mass distribution introduced by changing the battery in between test flights. The wind tunnel tests were conducted before the model identification flights, the data from which the HF models for the Beetle are

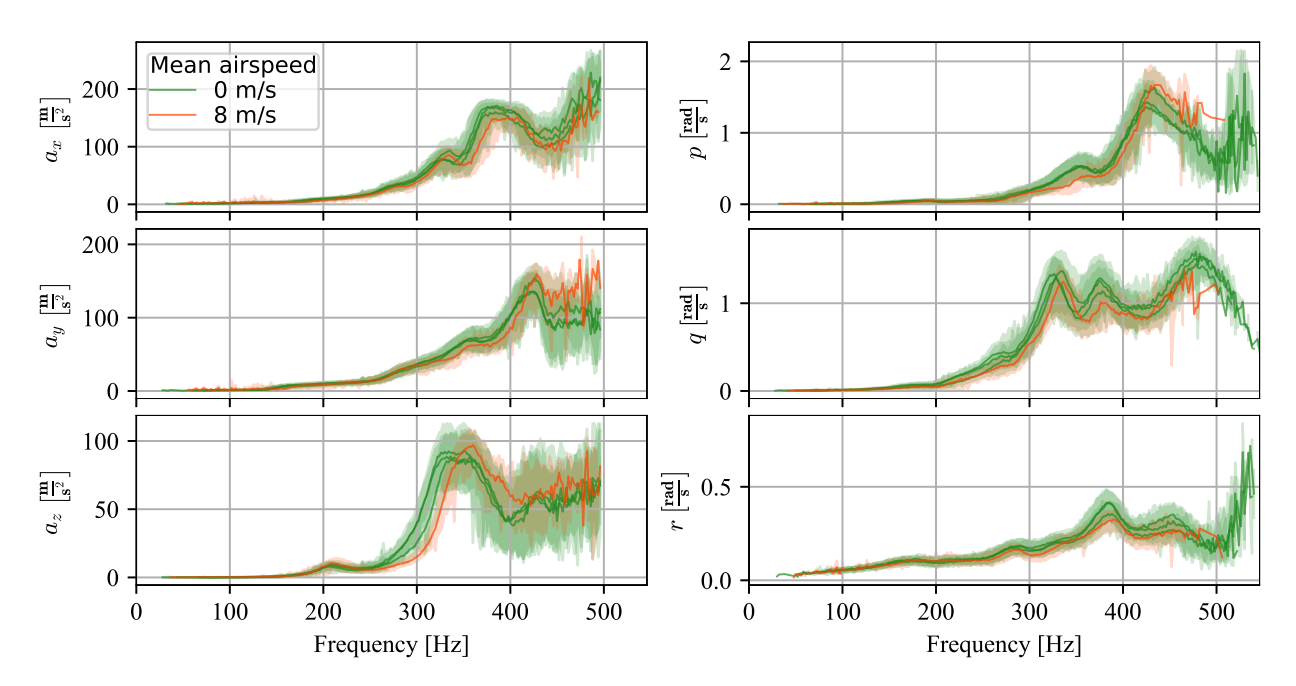


Fig. 33 First harmonic amplitude-frequency relationships of the Beetle quadrotor at varying wind speed for the same damage case (20FR)

constructed. For the latter, the battery was taped onto the airframe, and all flights were conducted with the same battery (recharged without detaching from the quadrotor). Therefore, the HF behavior is found to be very sensitive to even minor changes in the way the mass is distributed on the airframe. In fact, the variation of the high airspeed curve (red) in Fig. 33 may also largely be because of the fact that the battery was changed, and not purely because of the effect of flying at a higher mean airspeed.

While the amplitude-frequency relationships are modeled using simplex B-splines in the presented HF modeling methodology, an alternative approach would be to compute the frequency response function using pole-zero models. This has the potential advantage of providing fewer and more physical parameters that describe the local peaks and valleys observed in the amplitude curves as a function of frequency. However, this would come at the cost of providing a straightforward way to interpolate between the damage levels, which is a benefit of using the spline-based models.

Finally, the HF models are only constructed for the single damage case. If linearity is assumed, then a damage case for 2 simultaneously failed rotors can be simulated by adding the respective models corresponding to only one damaged rotor. The difference in phase between the two rotors in this case can cause constructive or destructive interference between the forces and moments created by each rotor. In a simulation, the angular positions of the rotors can be simulated through time integration, and so the dual damage cases can be simulated by simply super-imposing the models identified for single propeller damage. Clipping, especially in the simulated accelerometer, should be taken into account when simulating simultaneous damage in this way.

The super-imposition of single damage models would have to be validated through HF model identification of a quadrotor with simultaneous damage to two or more propellers. However, this presents further challenges. Since the rotor speeds are generally very close throughout most of the flight, spectral analysis through the STFT-based procedure described in this paper may not be applicable because the frequency resolution would be too low to differentiate the nearby frequencies. In this case, probably a single peak frequency corresponding to the dominant propeller can be extracted from the STFT, however, the amplitude of this peak would lump the influence of each damaged propeller. One remedy for this would be to fly maneuvers that create differences between rotor speeds such as aggressive pitch, roll, or yaw combined with simultaneous throttle punch maneuvers to ensure that the effects of imbalances in both propellers have significant amplitudes and sufficiently distanced frequencies.

C. Implications for blade damage diagnosis

Based on the aerodynamic models and high-frequency models identified for ABD, some important conclusions can also be drawn regarding the diagnosis of this damage case. High-frequency models are much more robust to the maneuvers because the primary dependence is on the (rotational) speed of the damaged rotor, while also being highly sensitive to the damage level. As shown in Sec. V.B.1, the HF behavior differs based on damage location, at the same damage level. Bondyra et al. [17] suggest that damage cannot be localized using only a single IMU, however, the results of this study show that this is not the case. A single IMU is a sensitive enough source of information to differentiate between the same level of damage at different locations. However, this sensitivity also comes with the disadvantage that two identically manufactured quadrotors may show significantly different HF model behavior. This also calls into question the various existing diagnosis methodologies [18, 21, 37] which rely purely on IMU data.

While the aerodynamic models suggest that online identification of these models may not be a good method for diagnosing damage, certain parameters such as the bias terms of the moment models, as well the parameter for the ω_{tot}^2 regressor for F_z offer a useful diagnostic tool which may not be as sensitive to the local variations in structural properties of the airframe like the HF models. However, these parameters would not provide information about the asymmetry of the damage, unlike the HF models. It may be possible to harness the strengths of both frequency regimes to develop a robust blade diagnosis framework that is robust to small changes between airframe properties of different quadrotors but can still provide accurate estimates of the type of blade damage present on the quadrotor.

VII. Conclusion

This paper explored the process of modeling the effects of asymmetric blade damage on the dynamics of a quadrotor. It was found that the effects can be largely separated into two frequency ranges, and modeled independently for each regime. Polynomial models constructed using stepwise regression, which quantify the effects of blade damage on the aerodynamic forces and moments were analyzed. These models were found to show good performance and were demonstrated to capture the effects of blade damage. However, the variations of parameter values as a function of damage extent were sporadic for most model regressors and therefore did not facilitate interpolation between damage levels, where experimental data is not gathered. A possible way to improve the aerodynamic model interpolatability would be to perform automated, and therefore more reproducible system identification flights at each damage level.

A novel approach for modeling the high-frequency effects of asymmetric blade damage in the frequency domain was developed. A simple sinusoidal model structure was found to capture a large part of the high-frequency behavior, producing accurate models of the HF phenomena, which also facilitated reasonably accurate interpolation of the HF behavior at damage levels not used for model identification. The HF modeling approach relies purely on onboard IMU measurements, therefore facilitating online identification. Additionally, with the approach being validated on two separate quadrotor platforms, the potential for generalization is demonstrated. The findings in terms of HF behavior also provide insights regarding the diagnosis of blade damage in quadrotors, or similar platforms. Primarily, the potential strengths and weaknesses of relying purely on IMU sensors as a source of information for diagnosis are highlighted. Future research should explore the development of robust blade damage diagnosis algorithms that fuse the high sensitivity capability of the IMU with more robust information provided by certain aerodynamic model terms such as the bias terms of aerodynamic moments, as well as the ω_{tot}^2 regressor for F_z .

Appendix A: IMU properties

This section presents and compares the noise properties of the MPU6000 and ICM42605 IMUs used for gathering experimental data. Additionally, the sampling jitter properties of both IMUs are also analyzed to examine the validity of using the STFT for spectral analysis, as it assumes constant sampling times.

Figure 34 shows the noise characteristics of the MPU6000 and ICM62605 IMUs. The distributions are constructed from 30 seconds of measurement data. While the gyroscopes perform similarly for both, the accelerometer measurements of the ICM42605 have significantly lower variances than the MPU6000. However, for the purposes of high-frequency model identification, the signal-to-noise ratio is very high for both IMUs for both accelerometer and gyroscope measurements. The data Note that the temperature was not recorded, however, the data was gathered under similar environmental conditions. It is therefore assumed that variation in temperature did not have a significant effect on the measured noise statistics.

Apart from the measurement noise, some jitter in sampling times was also observed in the raw IMU data for both the MPU6000 and ICM42605. Here a quantity *jitter fraction* (ϕ_j) is defined as per Eq. 39, where Δt_{true} is the

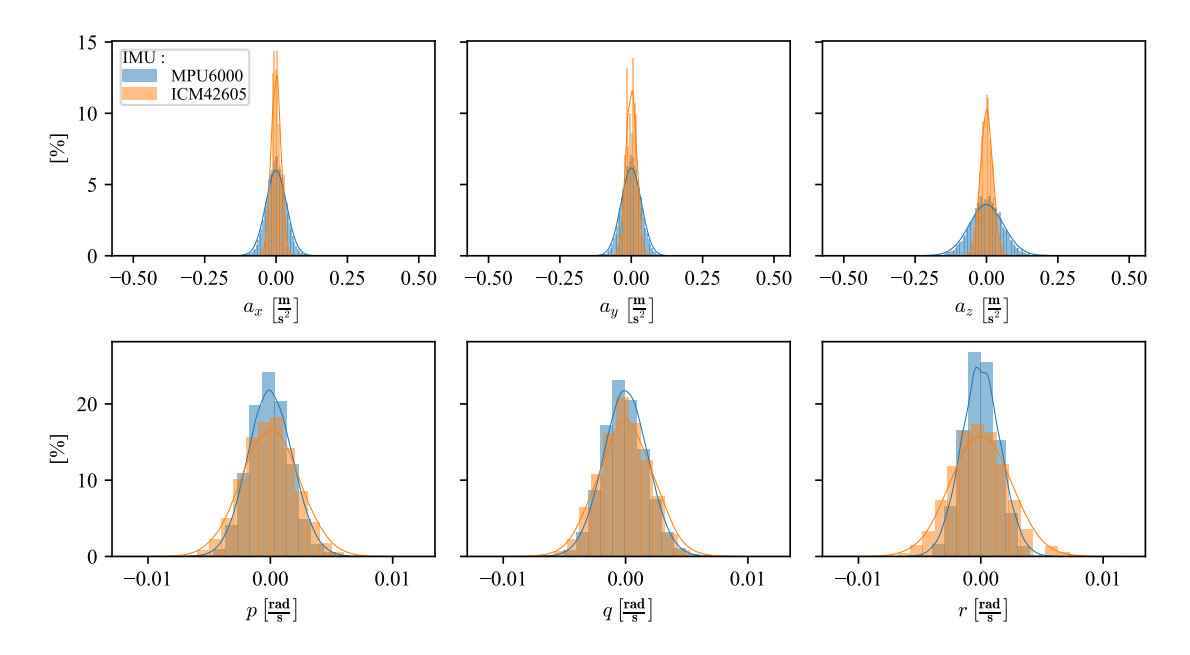


Fig. 34 Distributions of stationary noise measurements of the MPU6000 and ICM42605

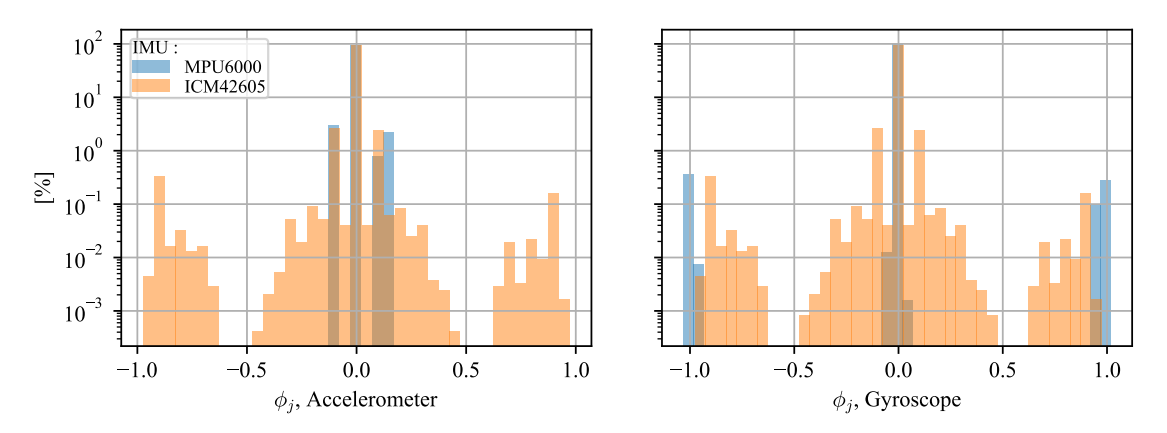


Fig. 35 Distributions of *jitter fraction* for the accelerometer (left) and gyroscope (right) measurements of the MPU6000 and ICM42605.

required sampling time and Δt_{meas} is the measured time difference between two consecutive samples. Figure 35 shows the distributions of phi_j for the accelerometer and gyroscope measurements. The raw IMU data in px4 is logged independently for the accelerometer and gyroscope, while the axes of both sensors are logged simultaneously. While there is some amount of sampling jitter, a vast majority of the measurements (>92%) show consistent sampling periods.

$$\phi_j = \frac{\Delta t_{true} - \Delta t_{meas}}{\Delta t_{true}} \tag{39}$$

Appendix B: Optimal STFT parameters based on signal properties

As discussed in the paper, the outputs of the STFT are highly sensitive to the choice parameters n_s and $n_{\rm fft}$, which are linked to the f_s , f_r , and f_{r_e} via Eq. 28 and 29 respectively. Intuitively, it is appropriate to assume that the choice of these parameters is influenced by the degree of non-stationarity of the sinusoidal signal to be analyzed, which can be formally defined as the maximum derivative of the frequency of the sinusoidal signal \dot{f}_{max} .

For the purpose of building the HF models presented in this paper, the sinusoidal IMU signals are analyzed using

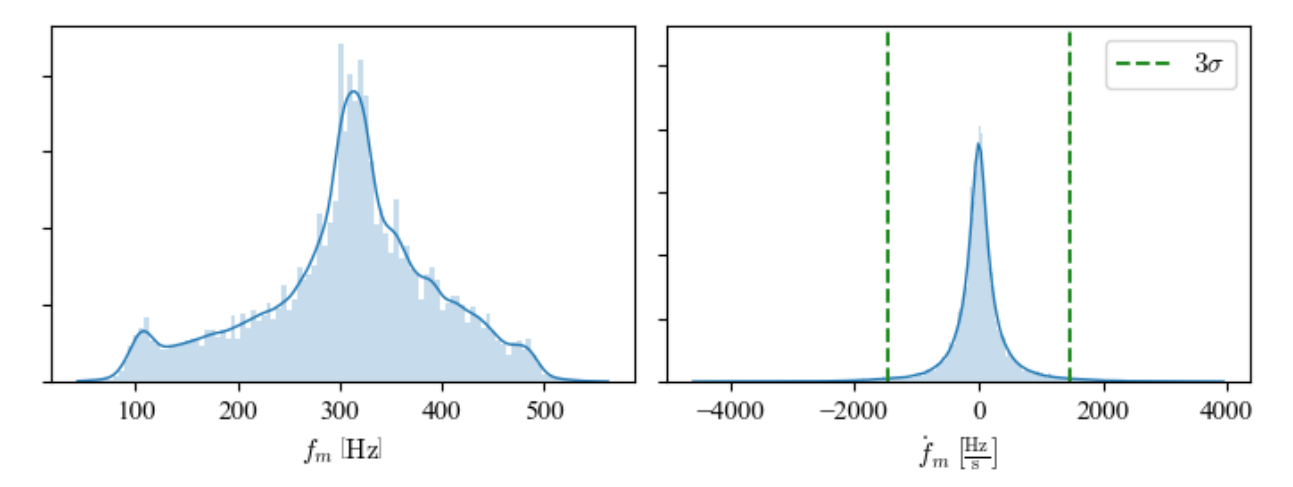


Fig. 36 Distribution of motor frequencies (left) and their derivative (right) constructed from data gathered from all Beetle test flights

the STFT. Because the frequency of these signals is directly related to the rotational frequency of the damaged propeller, it is useful to study the properties of the motor frequencies. Figure 36 shows the distributions of motor frequencies, and the derivatives of these frequencies, computed from the data of all the test cases presented in Table 3. We see that the sinusoidal signals measured by the IMU can have changes in frequency at more than 4000 Hz/s, however, very rare. A value of 2500 Hz/s for \dot{f}_{max} encompasses a large amount of the observed non-stationarity.

To determine a good choice for the parameters f_r and f_{r_e} , a numerical study was conducted. For this, artificial non-stationary sinusoidal signals are generated using Eq. 41 where the frequency of the signal is given by Eq. 40. The sampling rate of the test signal is chosen as 4 kHz, with a length of 20k samples, and the maximum f_{max} and minimum frequency f_{min} are chosen to be 1800 Hz and 100 Hz respectively. Then, the test signal is analyzed through the STFT at several combinations of f_r and frequency factor ψ_f (Eq. 42). The relative RMSE of the STFT-derived amplitude and frequency are computed, for each pair of f_r and ψ_f . Figure 37 shows the result of this process. It is clear from the results that a naive choice of parameters can lead to a very bad estimate of amplitude especially.

$$f(t) = \frac{f_{max} - f_{min}}{2} \sin\left(2\frac{\dot{f}_{max}}{f_{max} - f_{min}}t\right) + \frac{f_{max} - f_{min}}{2}$$
(40)

$$y(t) = \sin(2\pi f(t)) \tag{41}$$

$$\psi_f = \frac{f_{r_e}}{f_r} \tag{42}$$

While several good options for f_r and ψ_f are available, values of 60 Hz and 1/30 were chosen for each parameter respectively. This choice of parameters results in a very low error in both frequency (<2%) and amplitude (<5%) estimates derived from the STFT. Based on the definition of ψ_f , the chosen effective frequency resolution has a value of 2 Hz.

References

- [1] Cummings, A. R., McKee, A., Kulkarni, K., and Markandey, N., "The rise of UAVs," *Photogrammetric Engineering & Remote Sensing*, Vol. 83, No. 4, 2017, pp. 317–325.
- [2] Sun, S., Sijbers, L., Wang, X., and De Visser, C., "High-Speed Flight of Quadrotor Despite Loss of Single Rotor," *IEEE Robotics and Automation Letters*, Vol. 3, No. 4, 2018, pp. 3201–3207. https://doi.org/10.1109/LRA.2018.2851028.
- [3] Sun, S., Wang, X., Chu, Q., and de Visser, C., "Incremental nonlinear fault-tolerant control of a quadrotor with complete loss of two opposing rotors," *IEEE Transactions on Robotics*, Vol. 37, No. 1, 2020, pp. 116–130.
- [4] Mueller, M. W., and D'Andrea, R., "Stability and control of a quadrocopter despite the complete loss of one, two, or three propellers," 2014 IEEE international conference on robotics and automation (ICRA), IEEE, 2014, pp. 45–52.

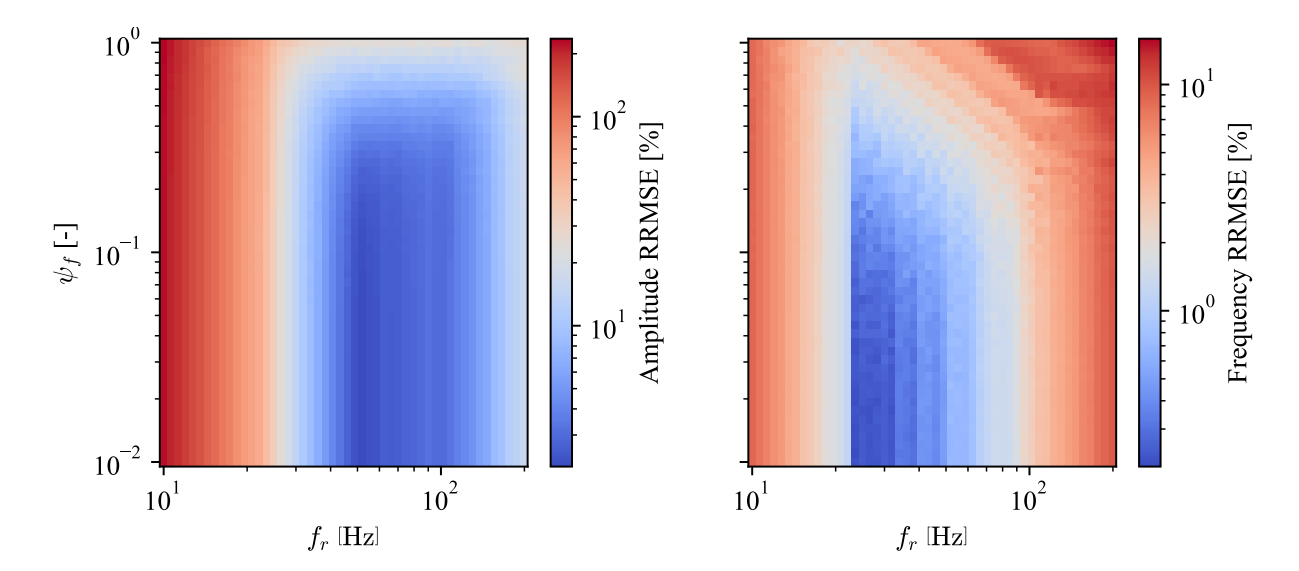


Fig. 37 Variation of STFT derived amplitude and frequency RRMSE a function of the frequency resolution f_r and the frequency factor ψ_f

- [5] Zhong, Y., Zhang, Y., Zhang, W., Zuo, J., and Zhan, H., "Robust actuator fault detection and diagnosis for a quadrotor UAV with external disturbances," *IEEE Access*, Vol. 6, 2018, pp. 48169–48180.
- [6] Amoozgar, M. H., Chamseddine, A., and Zhang, Y., "Experimental test of a two-stage Kalman filter for actuator fault detection and diagnosis of an unmanned quadrotor helicopter," *Journal of Intelligent & Robotic Systems*, Vol. 70, No. 1, 2013, pp. 107–117.
- [7] Sun, S., Schilder, R., and de Visser, C. C., "Identification of quadrotor aerodynamic model from high speed flight data," 2018 AIAA Atmospheric Flight Mechanics Conference, 2018, p. 0523.
- [8] Sun, S., "Quadrotor Fault Tolerant Flight Control and Aerodynamic Model Identification," Ph.D. thesis, Delft University of Technology, 2020. https://doi.org/10.4233/uuid:f0bdac3d-376d-4b24-9241-3a1e35731373.
- [9] Hoffmann, G. M., Huang, H., Waslander, S. L., and Tomlin, C. J., "Quadrotor helicopter flight dynamics and control: Theory and experiment," *Collection of Technical Papers - AIAA Guidance, Navigation, and Control Conference 2007*, Vol. 2, 2007, pp. 1670–1689. https://doi.org/10.2514/6.2007-6461.
- [10] Sun, S., and de Visser, C. C., "Quadrotor safe flight envelope prediction in the high-speed regime: A Monte-Carlo approach," AIAA Scitech 2019 Forum, 2019, p. 0948.
- [11] Avram, R. C., Zhang, X., and Muse, J., "Quadrotor sensor fault diagnosis with experimental results," *Journal of Intelligent & Robotic Systems*, Vol. 86, No. 1, 2017, pp. 115–137.
- [12] Guo, J., Qi, J., and Wu, C., "Robust fault diagnosis and fault-tolerant control for nonlinear quadrotor unmanned aerial vehicle system with unknown actuator faults," *International Journal of Advanced Robotic Systems*, Vol. 18, No. 2, 2021. https://doi.org/10.1177/17298814211002734.
- [13] Guo, K., Zhang, W., Zhu, Y., Jia, J., Yu, X., and Zhang, Y., "Safety Control for Quadrotor UAV against Ground Effect and Blade Damage," *IEEE Transactions on Industrial Electronics*, 2022. https://doi.org/10.1109/TIE.2022.3140494.
- [14] Asadi, D., Ahmadi, K., and Nabavi, S. Y., "Fault-tolerant Trajectory Tracking Control of a Quadcopter in Presence of a Motor Fault," *International Journal of Aeronautical and Space Sciences*, Vol. 23, No. 1, 2022, pp. 129–142. https://doi.org/10.1007/s42405-021-00412-9.
- [15] Sadeghzadeh, I., Mehta, A., and Zhang, Y., "Fault/damage tolerant control of a quadrotor helicopter UAV using model reference adaptive control and gain-scheduled PID," AIAA Guidance, Navigation, and Control Conference, 2011, p. 6716.

- [16] Guzmán-Rabasa, J. A., López-Estrada, F. R., González-Contreras, B. M., Valencia-Palomo, G., Chadli, M., and Pérez-Patricio, M., "Actuator fault detection and isolation on a quadrotor unmanned aerial vehicle modeled as a linear parameter-varying system," *Measurement and Control (United Kingdom)*, Vol. 52, No. 9-10, 2019, pp. 1228–1239. https://doi.org/10.1177/0020294018824764.
- [17] Bondyra, A., Gasior, P., Gardecki, S., and Kasiński, A., "Fault diagnosis and condition monitoring of UAV rotor using signal processing," 2017 Signal Processing: Algorithms, Architectures, Arrangements, and Applications (SPA), IEEE, 2017, pp. 233–238.
- [18] Yang, P., Wen, C., Geng, H., and Liu, P., "Intelligent fault diagnosis method for blade damage of quad-rotor uav based on stacked pruning sparse denoising autoencoder and convolutional neural network," *Machines*, Vol. 9, No. 12, 2021. https://doi.org/10.3390/machines9120360.
- [19] Brown, J. M., Coffey, J. A., Harvey, D., and Thayer, J. M., "Characterization and prognosis of multirotor failures," *Structural Health Monitoring and Damage Detection, Volume 7*, Springer, 2015, pp. 157–173.
- [20] Ghalamchi, B., Jia, Z., and Mueller, M. W., "Real-Time Vibration-Based Propeller Fault Diagnosis for Multicopters," IEEE/ASME Transactions on Mechatronics, Vol. 25, No. 1, 2020, pp. 395–405. https://doi.org/10.1109/TMECH.2019.2947250.
- [21] Du, C., Zhang, X., Zhong, R., Li, F., Yu, F., Rong, Y., and Gong, Y., "Unmanned aerial vehicle rotor fault diagnosis based on interval sampling reconstruction of vibration signals and a one-dimensional convolutional neural network deep learning method," *Measurement Science and Technology*, Vol. 33, No. 6, 2022. https://doi.org/10.1088/1361-6501/ac491e.
- [22] Liu, W., Chen, Z., and Zheng, M., "An audio-based fault diagnosis method for quadrotors using convolutional neural network and transfer learning," 2020 American Control Conference (ACC), IEEE, 2020, pp. 1367–1372.
- [23] Jiang, Y., Zhiyao, Z., Haoxiang, L., and Quan, Q., "Fault detection and identification for quadrotor based on airframe vibration signals: a data-driven method," 2015 34th chinese control conference (ccc), IEEE, 2015, pp. 6356–6361.
- [24] Smeur, E. J., Chu, Q., and De Croon, G. C., "Adaptive incremental nonlinear dynamic inversion for attitude control of micro air vehicles," *Journal of Guidance, Control, and Dynamics*, Vol. 39, No. 3, 2016, pp. 450–461.
- [25] Mahony, R., Kumar, V., and Corke, P., "Multirotor aerial vehicles: Modeling, estimation, and control of quadrotor," *IEEE Robotics and Automation Magazine*, Vol. 19, No. 3, 2012, pp. 20–32. https://doi.org/10.1109/MRA.2012.2206474.
- [26] Pounds, P., Mahony, R., and Corke, P., "Modelling and control of a quad-rotor robot," Proceedings of the 2006 Australasian Conference on Robotics and Automation, Australian Robotics and Automation Association (ARAA), 2006, pp. 1–10.
- [27] Bangura, M., Mahony, R., et al., "Nonlinear dynamic modeling for high performance control of a quadrotor," 2012.
- [28] Powers, C., Mellinger, D., Kushleyev, A., Kothmann, B., and Kumar, V., "Influence of aerodynamics and proximity effects in quadrotor flight," *Experimental robotics*, Springer, 2013, pp. 289–302.
- [29] Sun, S., De Visser, C. C., and Chu, Q., "Quadrotor gray-box model identification from high-speed flight data," *Journal of Aircraft*, Vol. 56, American Institute of Aeronautics and Astronautics Inc., 2019, pp. 645–661. https://doi.org/10.2514/1.C035135.
- [30] Prouty, R. W., Helicopter performance, stability, and Control, Krieger Publishing Company, 2002.
- [31] Sun, S., and de Visser, C., "Aerodynamic Model Identification of a Quadrotor Subjected to Rotor Failures in the High-Speed Flight Regime," *IEEE Robotics and Automation Letters*, Vol. 4, No. 4, 2019, pp. 3868–3875. https://doi.org/10.1109/lra.2019.2928758.
- [32] Morelli, E. A., and Klein, V., *Aircraft system identification: theory and practice*, Vol. 2, Sunflyte Enterprises Williamsburg, VA, 2016.
- [33] Ribeiro, M. I., "Kalman and extended kalman filters: Concept, derivation and properties," *Institute for Systems and Robotics*, Vol. 43, 2004, p. 46.
- [34] Jones, E., Oliphant, T., Peterson, P., et al., "SciPy: Open source scientific tools for Python,", 2001-. URL http://www.scipy.org/.
- [35] de Visser, C. C., Chu, Q., and Mulder, J., "A new approach to linear regression with multivariate splines," *Automatica*, Vol. 45, No. 12, 2009, pp. 2903–2909.
- [36] de Visser, C., Mulder, J., and Chu, Q., "Global nonlinear aerodynamic model identification with multivariate splines," *AIAA* atmospheric flight mechanics conference, 2009, p. 5726.

[37] Bondyra, A., Gasior, P., Gardecki, S., and Kasinski, A., "Development of the Sensory Network for the Vibration-based Fault Detection and Isolation in the Multirotor UAV Propulsion System," *ICINCO 2018 - Proceedings of the 15th International Conference on Informatics in Control, Automation and Robotics*, Vol. 2, SciTePress, 2018, pp. 102–109. https://doi.org/10. 5220/0006846801020109.